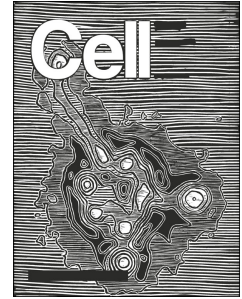


Journal Pre-proof



Genetic screens identify host factors for SARS-CoV-2 and common cold coronaviruses

Ruofan Wang, Camille R. Simoneau, Jessie Kulsuptrakul, Mehdi Bouhaddou, Katherine A. Travisano, Jennifer M. Hayashi, Jared Carlson-Stevermer, James R. Zengel, Christopher M. Richards, Parinaz Fozouni, Jennifer Oki, Lauren Rodriguez, Bastian Joehnk, Keith Walcott, Kevin Holden, Anita Sil, Jan E. Carette, Nevan J. Krogan, Melanie Ott, Andreas S. Puschnik

PII: S0092-8674(20)31626-3

DOI: <https://doi.org/10.1016/j.cell.2020.12.004>

Reference: CELL 11771

To appear in: *Cell*

Received Date: 26 September 2020

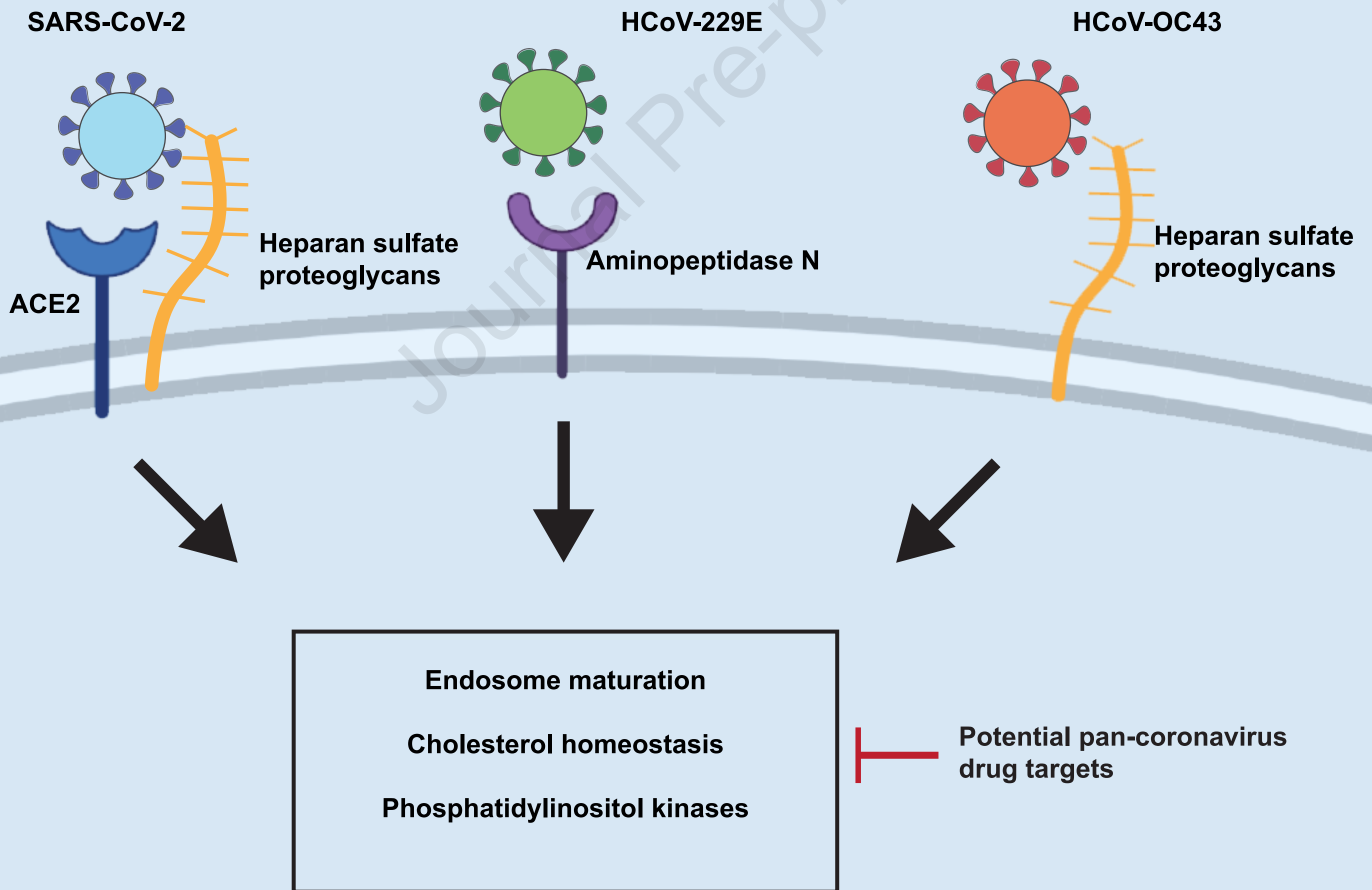
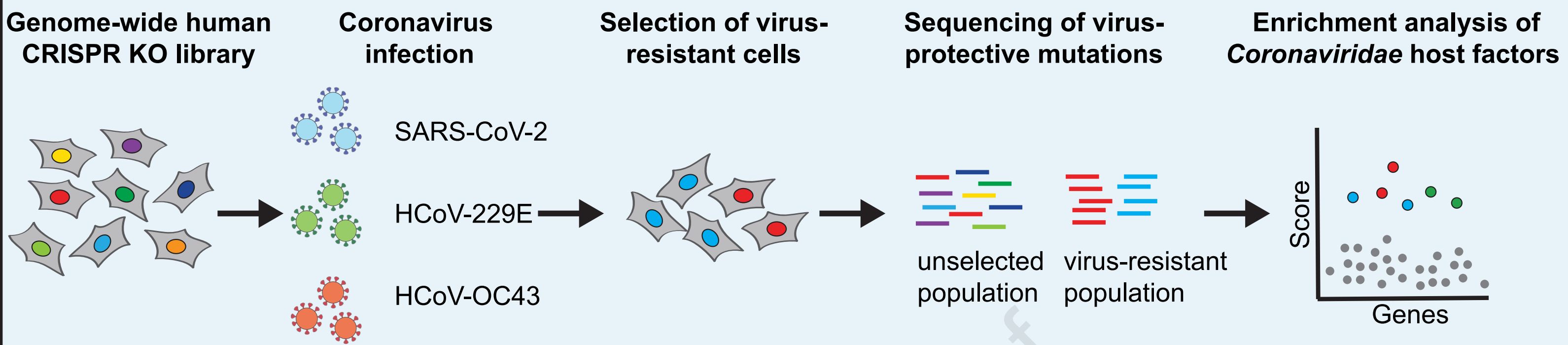
Revised Date: 13 November 2020

Accepted Date: 1 December 2020

Please cite this article as: Wang, R., Simoneau, C.R., Kulsuptrakul, J., Bouhaddou, M., Travisano, K.A., Hayashi, J.M., Carlson-Stevermer, J., Zengel, J.R., Richards, C.M., Fozouni, P., Oki, J., Rodriguez, L., Joehnk, B., Walcott, K., Holden, K., Sil, A., Carette, J.E., Krogan, N.J., Ott, M., Puschnik, A.S., Genetic screens identify host factors for SARS-CoV-2 and common cold coronaviruses, *Cell* (2021), doi: <https://doi.org/10.1016/j.cell.2020.12.004>.

This is a PDF file of an article that has undergone enhancements after acceptance, such as the addition of a cover page and metadata, and formatting for readability, but it is not yet the definitive version of record. This version will undergo additional copyediting, typesetting and review before it is published in its final form, but we are providing this version to give early visibility of the article. Please note that, during the production process, errors may be discovered which could affect the content, and all legal disclaimers that apply to the journal pertain.

© 2020 Elsevier Inc.



1 **Genetic screens identify host factors for SARS-CoV-2 and common cold**
2 **coronaviruses**

3
4 Ruofan Wang^{1,13}, Camille R. Simoneau^{2,3,4,5,13}, Jessie Kulsuptrakul¹, Mehdi
5 Bouhaddou^{2,4,6,7}, Katherine A. Travisano¹, Jennifer M. Hayashi^{2,3,4}, Jared Carlson-
6 Stevermer⁸, James R. Zengel⁹, Christopher M. Richards⁹, Parinaz Fozouni^{2,3,4,5,10},
7 Jennifer Oki⁸, Lauren Rodriguez¹¹, Bastian Joehnk¹², Keith Walcott¹², Kevin Holden⁸,
8 Anita Sil¹², Jan E. Carette⁹, Nevan J. Krogan^{2,4,6,7}, Melanie Ott^{2,3,4,*}, Andreas S.
9 Puschnik^{1,14,*}

10

11 ¹ Chan Zuckerberg Biohub, San Francisco, CA, 94158, USA

12 ² Gladstone Institutes, San Francisco, CA, 94158, USA

13 ³ Department of Medicine, University of California, San Francisco, CA, 94143, USA

14 ⁴ Quantitative Biosciences Institute COVID-19 Research Group (QCRG), University of
15 California, San Francisco, CA, 94158, USA

16 ⁵ Biomedical Sciences Graduate Program, University of California, San Francisco, CA,
17 94143, USA

18 ⁶ Quantitative Biosciences Institute (QBI), University of California, San Francisco, CA,
19 94158, USA

20 ⁷ Department of Cellular and Molecular Pharmacology, University of California, San
21 Francisco, CA, 94158, USA

22 ⁸ Synthego Corporation, Menlo Park, CA, 94025, USA

23 ⁹ Department of Microbiology and Immunology, Stanford University, Stanford, CA,
24 94305, USA

25 ¹⁰ Medical Scientist Training Program, University of California, San Francisco, CA,
26 94143, USA

27 ¹¹ UCSF CoLabs, Department of Microbiology and Immunology, University of California,
28 San Francisco, CA, 94143, USA

29 ¹² Department of Microbiology and Immunology, University of California, San Francisco,
30 CA, 94143, USA

31 ¹³ These authors contributed equally to this work

32 ¹⁴ Lead contact

33 * Correspondence: Melanie Ott, melanie.ott@gladstone.ucsf.edu, and Andreas S.
34 Puschnik, andreas.puschnik@czbiohub.org.

35 SUMMARY

36 The *Coronaviridae* are a family of viruses that cause disease in humans ranging from
37 mild respiratory infection to potentially lethal acute respiratory distress syndrome.
38 Finding host factors common to multiple coronaviruses could facilitate the development
39 of therapies to combat current and future coronavirus pandemics. Here, we conducted
40 genome-wide CRISPR screens in cells infected by SARS-CoV-2 as well as two
41 seasonally circulating common cold coronaviruses, OC43 and 229E. This approach
42 correctly identified the distinct viral entry factors ACE2 (for SARS-CoV-2),
43 aminopeptidase N (for 229E) and glycosaminoglycans (for OC43). Additionally, we
44 identified phosphatidylinositol phosphate biosynthesis and cholesterol homeostasis as
45 critical host pathways supporting infection by all three coronaviruses. By contrast, the
46 lysosomal protein TMEM106B appeared unique to SARS-CoV-2 infection.
47 Pharmacological inhibition of phosphatidylinositol kinases and cholesterol homeostasis
48 reduced replication of all three coronaviruses. These findings offer important insights for
49 the understanding of the coronavirus life cycle and the development of host-directed
50 therapies.

51

52 KEYWORDS

53 SARS-CoV-2, COVID-19, 229E, OC43, coronavirus, CRISPR, virus-host interactions,
54 host factors, host-targeted antivirals

55

56 INTRODUCTION

57 The *Coronaviridae* family includes seven known human pathogens, for which there are
58 no approved vaccines and only limited therapeutic options. The seasonally circulating
59 human coronaviruses (HCoV) OC43, HKU1, 229E and NL63 cause mild, common cold-
60 like, respiratory infections in humans (van der Hoek, 2007). However, three highly
61 pathogenic coronaviruses emerged in the last two decades, highlighting the pandemic
62 potential of this viral family (Drosten et al., 2003; Wu et al., 2020; Zaki et al., 2012).
63 Infection with severe acute respiratory syndrome coronavirus 1 (SARS-CoV-1) and
64 Middle East respiratory syndrome coronavirus (MERS-CoV) can lead to acute
65 respiratory distress syndrome and death, with fatality rates between 10-40% (Petersen
66 et al., 2020). SARS-CoV-2, though less deadly, is far more transmissible than SARS-
67 CoV-1 and MERS-CoV, and has been responsible for over 50 million cases and 1.2
68 million deaths globally as of November 2020 (Dong et al., 2020; Petersen et al., 2020).
69 Because of the severity of their impact on global health it is critical to understand how
70 SARS-CoV-2 and other coronaviruses hijack the host cell machinery during infection
71 and apply this knowledge to develop new therapeutic strategies.

72

73 Coronaviruses are enveloped, positive-sense, single-stranded RNA viruses with a
74 genome length of approximately 30kb. Upon receptor binding and membrane fusion, the
75 viral RNA is released into the cytoplasm, where it is translated to produce viral proteins.
76 Subsequently, the viral replication/transcription complexes form on double-membrane
77 vesicles and generate genome copies. These are then packaged into new virions via a
78 budding process, through which they acquire the viral envelope, and the resulting

79 virions are released from infected cells (Fung and Liu, 2019). During these steps,
80 specific cellular proteins are hijacked and play crucial roles in the viral life cycle. For
81 example, the angiotensin-converting enzyme 2 (ACE2) is exploited as the viral entry
82 receptor for NL63, SARS-CoV-1 and SARS-CoV-2 (Hofmann et al., 2005; Letko et al.,
83 2020; Li et al., 2003). Additionally, cellular proteases, such as TMPRSS2, cathepsin L
84 and furin are important for the cleavage of the viral spike (S) protein of several
85 coronaviruses thereby mediating efficient membrane fusion with host cells (Bertram et
86 al., 2013; Hoffmann et al., 2020b, 2020c; Shirato et al., 2013; Simmons et al., 2005).
87 Systematic studies have illuminated virus-host interactions during the later steps of the
88 viral life cycle. For example, proteomics approaches revealed comprehensive
89 interactomes between individual coronavirus proteins and cellular proteins (Gordon et
90 al., 2020a, 2020b; Stukalov et al., 2020). Additionally, biotin labelling identified
91 candidate host factors based on their proximity to coronavirus replicase complexes
92 (V'kovski et al., 2019). While these studies uncovered physical relationships between
93 viral and cellular proteins, they do not provide immediate information about the
94 importance of these host components for viral replication.

95

96 An orthogonal strategy is to screen for mutations that render host cells resistant to viral
97 infection using CRISPR-based mutagenesis. These screens identify host factors that
98 are functionally required for viral infection and could be targets for host-directed
99 therapies (Puschnik et al., 2017). In this study, we have performed a genome-wide
100 CRISPR knockout (KO) screen using SARS-CoV-2 (USA/WA-1 isolate) in human cells.
101 Importantly, we expanded our functional genomics approach to distantly related

102 *Coronaviridae* members in order to probe for commonalities and differences across the
103 family. This strategy can reveal potential pan-coronavirus host factors and thus
104 illuminate targets for antiviral therapy to combat the current and potential future
105 outbreaks. We conducted comparative CRISPR screens for SARS-CoV-2 and two
106 seasonally circulating common cold coronaviruses, OC43 and 229E. Our results
107 corroborate previously implicated host pathways, uncover new aspects of virus-host
108 interaction and identify targets for host-directed antiviral treatment.

109

110 **RESULTS**

111 **CRISPR knockout screens identify common and virus-specific candidate host** 112 **factors for coronavirus infection**

113 Phenotypic selection of virus-resistant cells in a pooled CRISPR KO screen is based on
114 survival and growth differences of mutant cells upon virus infection. We chose Huh7.5.1
115 hepatoma cells as they were uniquely susceptible to all tested coronaviruses. We
116 readily observed drastic cytopathic effect during OC43 and 229E infection (Figure S1A).
117 Huh7.5.1 also supported SARS-CoV-2 replication but exhibited limited virus-induced
118 cell death (Figures S1B and S1C). To improve the selection conditions for the SARS-
119 CoV-2 CRISPR screen, we overexpressed ACE2 and/or TMPRSS2, which are present
120 at low levels in WT Huh7.5.1 cells (Figure S1D). This led to increased viral uptake of a
121 SARS-CoV-2 spike-pseudotyped lentivirus, confirming the important function of ACE2
122 and TMPRSS2 for SARS-CoV-2 entry (Figure S1E). We ultimately used Huh7.5.1 cells
123 harboring a bicistronic *ACE2-IRES-TMPRSS2* construct for the SARS-CoV-2 screen as
124 these cells sustained efficient infection that led to widespread cell death while still

125 allowing the survival of a small number of cells (Figures S1C and S1F). The generated
126 CRISPR KO libraries in Huh7.5.1 and Huh7.5.1-*ACE2*-IRES-*TMPRSS2* cells had
127 virtually complete single-guide RNA (sgRNA) representation prior to the start of the
128 virus challenge but, as expected, were depleted of cells containing sgRNAs against
129 commonly essential fitness genes within 7 days post-library transduction (Figures S1G
130 and S1H) (Hart et al., 2015).

131
132 The three CRISPR screens - for resistance to SARS-CoV-2, 229E and OC43 - identified
133 a compendium of critical host factors across the human genome (Figure 1A and Table
134 S1). The overall performance of the screens was robust as indicated by the enrichment
135 of multiple individual sgRNAs against the top 10 scoring genes from each screen
136 (Figure S1I). Importantly, the known viral entry receptors ranked among the top hits:
137 *ACE2* for SARS-CoV-2 and aminopeptidase N (*ANPEP*) for 229E (Figures 1B and 1C)
138 (Letko et al., 2020; Yeager et al., 1992). OC43, unlike the other coronaviruses, does not
139 have a known proteinaceous receptor but primarily depends on sialic acid or
140 glycosaminoglycans for cell entry (Hulswit et al., 2019; Ströh and Stehle, 2014);
141 consistent with this fact, multiple heparan sulfate biosynthetic genes (*B3GALT6*,
142 *B3GAT3*, *B4GALT7*, *EXT1*, *EXT2*, *EXTL3*, *FAM20B*, *NDST1*, *SLC35B2*, *UGDH*,
143 *XYLT2*) were identified in our OC43 screen (Figures 1D and S2A). Several of these
144 genes were also markedly enriched in the SARS-CoV-2 screen (Figures 1B and S2A),
145 which is consistent with a recent report that SARS-CoV-2 requires both *ACE2* and
146 cellular heparan sulfate for efficient infection (Clausen et al., 2020). Overall, the

147 identification of the expected entry factors validates the phenotypic selection of our host
148 factor screens.

149

150 Gene Ontology (GO) enrichment analysis for each screen found a number of cellular
151 processes to be important for multiple coronaviruses. These processes included
152 proteoglycan and aminoglycan biosynthesis, vacuolar and lysosomal transport,
153 autophagy, Golgi vesicle transport and phosphatidylinositol metabolic processes (Figure
154 2A and Table S2).

155 In the phosphatidylinositol metabolic process, the SARS-CoV-2 screen identified
156 *VAC14*, which is part of the PIKfyve kinase complex (Figure 1B). *PIKFYVE* itself was
157 moderately enriched in the SARS-CoV-2 screen (Figure S2A). This complex catalyzes
158 the conversion of phosphatidylinositol-3-phosphate to phosphatidylinositol-3,5-
159 bisphosphate, which is localized to late endosomes (Shisheva, 2012). Interestingly, the
160 CRISPR screens with 229E and OC43 identified the subunits (*PIK3C3*, *UVRAG*,
161 *BECN1* and *PIK3R4*) of the class III phosphatidylinositol 3-kinase (PI3K) complex,
162 which generates the precursor phosphatidylinositol-3-phosphate in early endosome
163 membranes (Figures 1C, 1D and S2A) (Bilanges et al., 2019). Taken together, our data
164 highlight different steps of the phosphatidylinositol biosynthetic pathway, which
165 regulates endocytic sorting, endomembrane homeostasis and autophagy, to be critical
166 for the life cycle of all three and possibly all coronaviruses.

167

168 Another group of genes found in all three CRISPR screens is linked to cholesterol
169 metabolism. The SARS-CoV-2 resistant cell population contained multiple knockouts of

170 genes in the sterol regulatory element-binding protein (SREBP) pathway (*SCAP*,
171 *MBTPS1*, *MBTPS2*) (Figures 1B and S2A) (Brown et al., 2018). *SCAP* is an escort
172 protein for the transport of the transcription factors *SREBF1* and *SREBF2* from the ER
173 to the Golgi in response to low levels of cholesterol. In the Golgi, the *SREBF* proteins
174 are sequentially cleaved by the proteases *MBTPS1* and *MBTPS2*. Subsequently, the
175 transcription factors translocate to the nucleus to activate fatty acid and cholesterol
176 biosynthesis. *SREBF1* and *SREBF2* themselves did not score in the screen, potentially
177 due to their functional redundancy. *LDLR* (Low Density Lipoprotein Receptor), important
178 for cholesterol uptake, was enriched in both the SARS-CoV-2 and the 229E screen,
179 while *SCAP* was also enriched in the OC43 screen (Figures S2A and S2B). Additionally,
180 *NPC1* (Niemann–Pick intracellular cholesterol transporter 1), which facilitates export of
181 cholesterol from the endolysosomal compartment, ranked highly in the 229E screen
182 (Figure 1C) (Höglinger et al., 2019). Overall, our data indicate a strong link between
183 intracellular cholesterol levels and infection by all three coronaviruses.

184
185 Some genes were found in the OC43 and 229E screens, but not in the SARS-CoV-2
186 screen. For instance, the common cold coronavirus screens showed a strong overlap of
187 genes that are important for endosome and autophagosome maturation (Figures 1C, 1D
188 and S2B). These include *RAB7A*, components of the HOPS complex (encoded by
189 *VPS11*, *VPS16*, *VPS18*, *VPS33A*), the Ccz1-Mon1 guanosine exchange factor complex
190 (encoded by *CCZ1*, *CCZ1B*, *C18orf8*), genes expressing the WDR81-WDR91 complex,
191 and other genes related to lysosome and autophagosome function (*SPNS1*, *TOLLIP*,
192 *TMEM41B*, *AMBRA1*) (Balderhaar and Ungermann, 2013; Hegedűs et al., 2016;

193 Hoffmann et al., 2020a; Katoh et al., 2004; Maria Fimia et al., 2007; Moretti et al., 2018;
194 Rapiteanu et al., 2016; Rong et al., 2011). We also identified cathepsin L (CTSL1) as
195 well as the mannose-6-phosphate receptor (M6PR) and GNPTAB, which are important
196 for proper trafficking of lysosomal enzymes from the trans-Golgi network (Flint et al.,
197 2019; Saftig and Klumperman, 2009). Interestingly, the HOPS complex, cathepsins,
198 GNPTAB and SPNS1 were previously linked to Ebola virus entry, implying similar viral
199 entry strategies (Carette et al., 2011; Flint et al., 2019).

200

201 The OC43 and 229E screens also uncovered KEAP1, the principal negative regulator of
202 NRF2, whose activation restores cellular redox and protein homeostasis (Figures 1C
203 and 1D) (Cuadrado et al., 2019). Activation of the NRF2 transcriptional program may
204 induce a cellular state that is protective against coronavirus infection. Indeed, NRF2
205 agonists seem to elicit an antiviral response as demonstrated in cell culture and were
206 proposed for SARS-CoV-2 treatment (Cuadrado et al., 2020; Olganier et al., 2020).

207

208 In addition to genes that scored in multiple CRISPR screens, we also found genes that
209 were only enriched in one screen. Several genes related to the Golgi apparatus were
210 uncovered only in the 229E screen and may possibly have 229E-specific roles. Among
211 them were *GPR89A* and *GPR89B*, which encode two highly homologous G protein
212 coupled receptors important for Golgi acidification (Maeda et al., 2008), and NBAS and
213 USE1, which play a role in Golgi-to-ER retrograde transport (Aoki et al., 2009). The
214 exact role of these factors in coronavirus infection – and their specificity to 229E –
215 remain to be determined.

216

217 The SARS-CoV-2 screen identified multiple subunits of the exocyst (EXOC1-8) (Figures
218 1B and S2A), an octameric protein complex that facilitates the tethering of secretory
219 vesicles to the plasma membrane prior to SNARE-mediated fusion (Mei and Guo,
220 2018). This complex could therefore facilitate trafficking of virus particles during entry or
221 egress, or regulate surface expression of viral entry factors. The top hit of the SARS-
222 CoV-2 screen was TMEM106B, a poorly characterized lysosomal transmembrane
223 protein linked to frontotemporal dementia (Figure 1B) (Lüningschrör et al., 2020).
224 Deletions in TMEM106B have been shown to cause defects in lysosome trafficking,
225 impaired acidification and reduced levels of lysosomal enzymes but its precise
226 molecular function remains enigmatic (Klein et al., 2017; Lüningschrör et al., 2020).
227 *TMEM106B* knockout could thus affect SARS-CoV-2 entry, although it is also possible
228 to protect from virus-induced cell death at other stages of the life cycle.

229

230 Overall, the comparative CRISPR screen strategy provides a rich list of shared and
231 distinct candidate host factors for subsequent validation and host-directed inhibition of
232 coronavirus infection.

233

234 **Network propagation across multiple CRISPR screens highlights functional** 235 **biological clusters important for coronavirus infection**

236 To expand upon our manual curated analysis, which highlighted top-scoring genes from
237 each coronavirus screen, we employed a network propagation approach using the
238 entirety of our unthresholded datasets to better understand the functional connections

239 between the genes identified in our screens (Cowen et al., 2017). This approach
240 allowed us to identify molecular networks that emerge from our datasets even if certain
241 gene members fell below our top-scoring threshold. Network propagation is a powerful
242 technique that uses a 'guilt-by-association' approach to propagate biological signal
243 within large networks (e.g. Pathway Commons) to identify interconnected neighborhood
244 clusters or pathways. In addition to revealing the functional networks underlying a
245 particular dataset, this approach can be especially useful for identifying converging
246 molecular networks across datasets. Here, we used an integrative network propagation
247 approach to identify subnetworks and pathways that were common across the three
248 coronavirus screens (Figure 2B). Briefly, we propagated the unthresholded CRISPR
249 screen enrichment scores from each coronavirus screen and utilized a statistical
250 permutation test paired with network clustering methods to extract network
251 neighborhoods implicated across all three coronavirus screens.

252

253 Propagations from the three CRISPR screens identified subnetworks most common to
254 all three viruses and independently confirmed the biological processes highlighted as
255 important for coronavirus infection in our previous analysis (Figures 2C, S3A and S3B,
256 Tables S2 and S3). For instance, we found clusters linked to cholesterol metabolism
257 (containing SCAP, MBTPS1, SREBF2, LDLR and NPC1), endosome to lysosome
258 transport (including the HOPS complex components VPS11, VPS16, VPS18, VPS33A
259 and VPS39) and glycoprotein biosynthetic processes (containing heparan sulfate
260 biosynthesis genes). Another cluster reflected the critical role of autophagy/

261 phospholipid metabolism and indicated a functional link between VAC14 and subunits of
262 the PI3K complex as described above.

263

264 Moreover, network propagation also identified previously unappreciated biological
265 functions, such as steroid hormone signaling, cell-cell adhesion, metal ion transport,
266 intra-Golgi vesicle transport, snare complex assembly, Rab protein signal transduction,
267 peroxisomal transport and mRNA splicing (Figures 2C, S3A and S3B, Tables S2 and
268 S3). Interestingly, some of these processes were also implicated by recent coronavirus
269 interactome studies (Gordon et al., 2020a, 2020b). We therefore additionally compared
270 our CRISPR screen results with the hits from the SARS-CoV-2 interactome revealing
271 SCAP, several Rab proteins and HOPS complex subunits as functionally relevant for
272 infection as well as interactors with viral proteins (Figure S2C). Altogether, the network
273 propagation and cross-comparison with the protein interaction network highlighted
274 numerous distinct cellular processes that may have critical roles during coronavirus
275 infection.

276

277 **Knockout of candidate host factor genes reduces coronavirus replication**

278 To validate the candidate genes from the SARS-CoV-2 screen, we generated individual
279 KO cells in three cell types. We introduced gene deletions for several top hits in A549
280 lung epithelial cells transduced with *ACE2* (A549-*ACE2*) using Cas9 ribonucleoproteins
281 (RNPs), resulting in high indel frequencies (Table S4). SARS-CoV-2 RNA levels were
282 markedly reduced in A549-*ACE2* cells that contained mutations in *ACE2*, ADP
283 Ribosylation Factor 5 (*ARF5*), multiple subunits of the exocyst (*EXOC2*, *EXOC6*,

284 *EXOC8*), the cholesterol homeostasis genes *SCAP*, *MBTPS1* and *MBTPS2*, the
285 phosphatidylinositol kinase complex genes *PIKFYVE* and *VAC14*, or *TMEM106B*
286 (Figure 3A). Next, we lentivirally introduced Cas9 and sgRNAs against a subset of these
287 genes (*TMEM106B*, *VAC14*, *SCAP*, *MBTPS2*, *EXOC2*) into Calu-3 lung epithelial cells
288 with endogenous ACE2 levels and also observed reduced viral replication compared to
289 control cells harboring a non-targeting sgRNA (Figure 3B).

290 Lastly, we generated clonal Huh7.5.1 cells (without *ACE2-IRES-TMPRSS2*
291 overexpression) containing frameshift mutations in candidate genes, resulting in loss of
292 protein expression (Figures S4A and S4B). Deletion of *TMEM106B* and *VAC14*
293 decreased SARS-CoV-2 replication, and this effect was reversed by add-back (AB) of
294 respective cDNAs (Figures 3C, 3D and S4B), confirming the role of these two factors in
295 the SARS-CoV-2 life cycle. Similarly, knocking out *SCAP*, *MBTPS2* or *EXOC2* led to a
296 decrease of SARS-CoV-2 RNA levels (Figure 3E). When we infected the same
297 Huh7.5.1 KO cells with OC43 and 229E, we observed reduced viral replication in *SCAP*,
298 *MBTPS2* and *EXOC2* KO cells but not in *TMEM106B* KO and only moderately in
299 *VAC14* KO cells (Figure 3F). This suggests that the latter genes are more rate-limiting
300 in SARS-CoV-2 infection.

301

302 Next, we probed Huh7.5.1 cells lacking genes involved in endosome maturation or the
303 PI3K complex, which were initially found in the common cold coronavirus screens. We
304 saw reduced viral replication for OC43 and 229E (Figures 3G and 3H). Additionally, we
305 observed increased cell viability in all KO cells relative to WT Huh7.5.1 cells 8 dpi
306 (Figures S4C and S4D), indicating that these genes are important for infection by the

307 common cold viruses and for virus-induced cell death. We then tested whether the hits
308 shared between OC43 and 229E affect SARS-CoV-2. Indeed, SARS-CoV-2 infection
309 was reduced in cells lacking certain endosomal or PI3K genes in the context of
310 Huh7.5.1 without *ACE2-IRES-TMPRSS2*, similar to the common cold coronaviruses
311 (Figure 3I). Complementation of *PIK3R4* and *VPS16* KO cells with respective cDNAs
312 restored SARS-CoV-2 and 229E, and to a lesser degree, OC43 replication levels
313 (Figures 3J-O and S4B). To rule out the possibility that decreased viral replication is not
314 due to severe cellular growth defects, we measured proliferation of RNP-edited A549-
315 ACE2 and clonal Huh7.5.1 KO cells. Apart from *SCAP* KO cells we did not observe any
316 notable growth differences compared to WT cells (Figures S4E and S4F).
317 Together, these experiments confirm that the host factors identified in our screens in
318 Huh7.5.1 cells have functional roles for *Coronaviridae*, which are also relevant in lung
319 epithelial cells. Furthermore, we demonstrated that important aspects of SARS-CoV-2
320 biology can be revealed by studying the common cold coronaviruses.

321

322 **Compounds directed at host factors inhibit coronavirus replication**

323 Host factors important for virus infection are potential targets for antiviral therapy. Host-
324 directed therapy is advantageous as it allows pre-existing drugs to be repurposed, may
325 provide broad-spectrum inhibition against multiple viruses, and is generally thought to
326 be more refractory to viral escape mutations than drugs targeting viral factors
327 (Bekerman and Einav, 2015). We therefore explored whether the cellular pathways
328 identified in our screens could serve as targets for therapy against coronavirus infection.

329

330 Given the strong dependence of all three coronaviruses on *PIK3R4*, we tested SAR405,
331 a selective and ATP-competitive inhibitor of class III PI3K (PIK3C3) (Ronan et al.,
332 2014). The drug exhibited a dose-dependent effect against all three coronaviruses with
333 low cytotoxicity in Huh7.5.1 cells, which is consistent with the reduced virus replication
334 in *PIK3R4* KO cells and suggests that SAR405 could serve as a pan-coronavirus
335 inhibitor (Figures 4A-C). As VAC14, a PIKfyve complex component, was a strong hit in
336 the SARS-CoV-2 screen, we also tested the PIKfyve inhibitor YM201636 and observed
337 inhibition of SARS-CoV-2 replication (Figure S5A) (Jefferies et al., 2008). Similar
338 antiviral activity was previously demonstrated with apilimod, another PIKfyve inhibitor
339 (Bouhaddou et al., 2020; Kang et al., 2020; Ou et al., 2020).

340
341 Furthermore, we tested compounds modulating cholesterol homeostasis as this
342 pathway also appeared important for all three coronaviruses. PF-429242, a reversible,
343 competitive aminopyrrolidineamide inhibitor of MBTPS1 showed strong dose-dependent
344 reduction of SARS-CoV-2, 229E and, to lesser degree, OC43 replication with
345 cytotoxicity only at high concentration (Figures 4D-F) (Hawkins et al., 2008). 25-
346 Hydroxycholesterol (25-HC), which promotes ER retention of the SCAP–SREBP
347 complex (Brown et al., 2018), also potently reduced replication of all three
348 coronaviruses (Figures 4G-I). Fatostatin, which binds to SCAP and inhibits ER-to-Golgi
349 translocation of SREBPs (Kamisuki et al., 2009), moderately reduced SARS-CoV-2
350 infection levels at higher doses (Figure S5B). We confirmed on-target activity of the
351 SREBP pathway modulators by measuring reduced expression of SREBP-regulated
352 genes upon drug treatment (Figure S5C).

353

354 We also tested Bardoxolone, an activator of the KEAP1-NRF2 complex (Liby and
355 Sporn, 2012), since KEAP1 scored highly in both common cold coronavirus screens.
356 Bardoxolone potently inhibited 229E and OC43 replication and also reduced SARS-
357 CoV-2 RNA levels at slightly higher concentrations (Figures 4J-L), suggesting potential
358 pan-coronaviral activity.

359

360 Finally, we confirmed the inhibitory effects of the different compounds against SARS-
361 CoV-2 replication in Calu-3 cells; viral RNA levels were markedly suppressed without
362 notable cytotoxicity (Figures S5D and S5E). Therefore, our genetic and pharmacological
363 studies provide new targets for potential pan-coronavirus host-directed therapies that
364 may be explored further *in vivo*.

365

366 **Cellular cholesterol is important for spike-mediated entry of SARS-CoV-2**

367 Next, we tested whether some of the identified genes affect viral entry. We generated a
368 clonal Huh7.5.1-*ACE2/TMPRSS2* overexpression cell line to facilitate efficient infection
369 with a SARS-CoV-2 spike pseudotyped vesicular stomatitis virus (VSV-SARS-CoV-2-S)
370 expressing GFP, which can be utilized to specifically probe effects on spike-mediated
371 entry of SARS-CoV-2. We then introduced Cas9 RNPs and created knockout lines for
372 our genes of interest. Editing efficiencies were high and loss of protein was confirmed
373 for *TMEM106B* (Figures 5A and Table S4). As expected, knockout of *ACE2* drastically
374 reduced infection with VSV-SARS-CoV-2-S (Figure 5B). By contrast, we did not observe
375 a decrease of viral entry in *TMEM106B* and *VAC14* KO cells, suggesting that they do

376 not play a role in spike-mediated entry (Figure 5B). We saw reduced uptake of
377 pseudotyped viral particles in all cells with knockouts in cholesterol-related genes
378 (*SCAP*, *MBTPS1*, *MBTPS2*) as well as a modest decrease in exocyst deficient cells
379 (Figure 5B). Finally, to examine whether treatment with cholesterol inhibitors also
380 prevents viral entry similar to the genetic perturbations, we pretreated Huh7.5.1-
381 *ACE2/TMPRSS2* cells with different concentrations of PF-429242 or 25-HC and
382 measured pseudotyped virus infection. Both drugs exhibited a dose-dependent
383 reduction of infection levels (Figures 5C and 5D), suggesting that cellular cholesterol is
384 required for efficient spike-mediated entry of SARS-CoV-2.

385

386 **DISCUSSION**

387 In this study, we performed genome-scale CRISPR KO screens to identify host factors
388 important for SARS-CoV-2, 229E and OC43. Our data highlight that while the three
389 coronaviruses exploit distinct entry factors, they also depend on a convergent set of
390 host pathways, with potential roles for the entire *Coronaviridae* family.

391

392 In particular, genes involved in cholesterol homeostasis were enriched in all of our
393 screens and in the network propagation. Two recent SARS-CoV-2 interactome maps
394 have also revealed binding of viral proteins to the cholesterol regulator SCAP (Gordon
395 et al., 2020a; Stukalov et al., 2020); given the essentiality of SCAP for infection, the
396 interacting viral proteins are likely to positively regulate SCAP activity and cholesterol
397 levels. Interestingly, two clinical studies found improved outcomes for COVID-19
398 patients treated with cholesterol reducers statins (Daniels et al., 2020; Zhang et al.,

399 2020). Mechanistically, our genetic and pharmacological experiments showed that
400 SARS-CoV-2 requires cellular cholesterol for efficient entry. This observation is also
401 supported by a recent screen for interferon-stimulated genes that protect from SARS-
402 CoV-2 infection, which identified cholesterol 25-hydroxylase (CH25H) as one of the top
403 hits (Zang et al., 2020). Cholesterol homeostasis has also been linked to viral entry and
404 membrane fusion in the context of bunya- and hantavirus infections, suggesting a pro-
405 viral function across different viral families (Charlton et al., 2019; Kleinfelter et al., 2015;
406 Petersen et al., 2014).

407
408 Our screens also uncovered phosphatidylinositol biosynthesis as an important pathway
409 for coronavirus infection. While PIKfyve kinase has previously been implicated through
410 chemical inhibition (Bouhaddou et al., 2020; Kang et al., 2020; Ou et al., 2020), which is
411 consistent with our identification of VAC14, we also found the upstream PI3K complex
412 as a new critical host factor that may exhibit pan-coronavirus function. Due to its
413 involvement in multiple cellular processes including vesicular trafficking and autophagy
414 (Bilanges et al., 2019), it remains to be determined whether coronaviruses hijack the
415 PI3K pathway during entry and/or for the generation of double-membrane vesicles
416 required for the viral replication/transcription complexes. Our results also inform those of
417 a recent drug repurposing screen that identified ~100 compounds that inhibited SARS-
418 CoV-2 replication (Riva et al., 2020); notably, among those were PIKfyve inhibitors,
419 protease inhibitors and modulators of cholesterol homeostasis. Our functional genomics
420 data therefore suggest that the observed effects of these compounds were possibly due
421 to inhibition of critical host factors.

422

423 While this study was under review, several other SARS-CoV-2 CRISPR screen studies
424 were published or deposited as preprints, revealing important aspects of the viral life
425 cycle (Baggen et al., 2020; Daniloski et al., 2020; Schneider et al., 2020; Wei et al.,
426 2020; Zhu et al., 2020). Our screen for SARS-CoV-2 host factors using Huh7.5.1-ACE2-
427 IRES-TMPRSS2 cells identified the known SARS-CoV-2 entry factors, such as ACE2
428 and heparan sulfate, supporting its validity. Additional notable candidate host factors are
429 TMEM106B, VAC14, cholesterol regulators and subunits of the exocyst. Remarkably,
430 the majority of these genes were independently identified in a CRISPR screen using
431 Huh7.5 cells, the parental line of the Huh7.5.1 cells we used in our study, underscoring
432 the reproducibility and importance of these host factors for SARS-CoV-2 infection
433 (Schneider et al., 2020). TMEM106B was additionally found in a third study (Baggen et
434 al., 2020). While the exact molecular function of TMEM106B for SARS-CoV-2 infection
435 remains to be determined, its importance was confirmed in several in cell lines
436 (including lung cells) by Baggen et al. and our study.

437

438 By contrast, many of the host factors we found to be essential were missed by the other
439 recently published studies (Daniloski et al., 2020; Wei et al., 2020; Zhu et al., 2020),
440 possibly due to the different chosen experimental systems. Wei et al. performed
441 genome-wide CRISPR screens in the African green monkey cell line VeroE6. Besides
442 the bona fide entry factors ACE2 and cathepsin L, the screen largely revealed
443 chromatin modifiers such as HMGB1 and the SWI/SNF chromatin remodeling complex
444 (Wei et al., 2020). The former was shown to regulate transcription of ACE2, thereby

445 indirectly modulating susceptibility to SARS-CoV-2 infection in VeroE6. HMGB1 was not
446 markedly enriched in any of the CRISPR screens conducted in human cells, suggesting
447 that regulation of receptor expression levels may be species- or cell type-dependent.
448 Daniloski et al. and Zhu et al. conducted their screens in A549-ACE2 cells. Both studies
449 identified ACE2, cathepsin L and genes related to endosome acidification (e.g. subunits
450 of the V-ATPase) or endosomal protein sorting and recycling (RAB7A, retromer
451 complex, commander complex, WASH complex) (Daniloski et al., 2020; Zhu et al.,
452 2020). The latter were shown to be critical for ACE2 cell surface expression and
453 therefore likely to affect viral entry indirectly.

454
455 There is emerging evidence that SARS-CoV-2 entry can occur through different
456 “routes”, depending on the level of TMPRSS2 on target cells as well as on mutations in
457 the polybasic S1/S2 site of the viral spike protein (Hoffmann et al., 2020b, 2020c; Zhu et
458 al., 2020). The cleavage of SARS-CoV-2 spike can occur either at the plasma
459 membrane via TMPRSS2 or in endolysosomes through cathepsins. Sufficient
460 TMPRSS2 levels may thus ablate the requirement for cathepsin and other factors linked
461 to endolysosomal activity, a hypothesis supported by our screen, which was carried out
462 in the context of TMPRSS2 overexpression and did not uncover cathepsins as crucial
463 host factors. By contrast, A549 and VeroE6 cells do not express detectable TMPRSS2
464 levels, and the virus may thus rely preferentially on cathepsins for entry as screens in
465 these cells indicate (Daniloski et al., 2020; Matsuyama et al., 2020; Wei et al., 2020;
466 Zhu et al., 2020). However, nasal and lung epithelial cells, the natural target cells of
467 SARS-CoV-2, can express high levels of TMPRSS2 (Sungnak et al., 2020). We

468 therefore speculate that the genes identified in our SARS-CoV-2 CRISPR screen using
469 Huh7.5.1-ACE2-IRES-TMPRSS2 cells are physiologically relevant to SARS-CoV-2
470 infection *in vivo*.

471

472 In summary, our study presents a screen for host factors carried out in a TMPRSS2-
473 positive genetic background. It therefore unveils host factors critical for SARS-CoV-2
474 infection that may be more physiologically relevant than those uncovered so far in other
475 genetic backgrounds. In addition, our comparative screens highlight commonalities and
476 differences between SARS-CoV-2 and the common cold coronaviruses OC43 and
477 229E. In particular, this comparison led to the identification of the PI3K complex and
478 cholesterol homeostasis as targets to pursue for the development of host-directed, pan-
479 coronaviral therapy.

480 ACKNOWLEDGMENTS

481 This research was funded by grants from the National Institutes of Health
482 (R01AI140186-S and R01AI141970 to J.E.C.; P50AI150476, U19AI135990,
483 U19AI135972, R01AI143292, R01AI120694, P01A1063302, and R01AI122747 to
484 N.J.K.; F32CA239333 to M.B.; 5DP1DA038043 to M.O.). J.E.C. was also supported by
485 a pilot grant from Stanford ChEM-H Innovative Medicines Accelerator (IMA). M.O.
486 acknowledges support through a gift from the Roddenbury. Funding to A.S.P. was
487 provided by the Chan Zuckerberg Biohub. We would like to thank Dr. Nathan Meyers for
488 laboratory support; Matthew Laurie for help with Bravo liquid handling; Anke Meyer-
489 Franke for help with automated microscopy; Michelle Tan, Angela Detweiler and Norma
490 Neff for help with sequencing; Dr. Sandra Schmid, Dr. Don Ganem and Dr. Francoise
491 Chanut for editorial comments; Dr. Olga Gulyaeva, Sara Sunshine, Dr. Marco Hein, and
492 Dr. Scott Biering for helpful discussion. We also express gratitude to the Biohub lab
493 management and operations team for their support.

494

495 AUTHOR CONTRIBUTIONS

496 R.W., C.R.S., J.K., K.A.T., J.M.H., J.C.S., J.R.Z., C.M.R., P.F., J.O., L.R. and A.S.P.
497 performed experiments. R.W., C.R.S., J.K., K.A.T., J.M.H., J.C.S., J.R.Z., C.M.R. and
498 A.S.P. designed experiments. R.W., C.R.S., J.K., M.B., K.A.T., J.M.H., J.C.S., J.R.Z.
499 and A.S.P. analyzed and visualized data. L.R., B.J., K.W. and A.S. provided BSL-3
500 laboratory support and training. K.H., A.S., J.E.C., N.J.K., M.O. and A.S.P. supervised
501 study and provided technical guidance. A.S.P. conceptualized study and wrote initial

502 draft of the manuscript. R.W., C.R.S., M.B., K.A.T., J.M.H., J.C.S., J.R.Z., J.E.C., N.J.K.,
503 and M.O. provided comments and edits on the manuscript.

504

505 **DECLARATION OF INTERESTS**

506 J.C.S., J.O. and K.H. are employees of Synthego Corporation. All authors declare no
507 other competing interests.

Journal Pre-proof

508 **MAIN FIGURE TITLES AND LEGENDS**

509 **Figure 1: Genome-wide loss-of-function screens in human cells identify host**
510 **factors important for infection by SARS-CoV-2, 229E and OC43.**

511 **(A)** Schematic of CRISPR-based KO screens for the identification of coronavirus host
512 factors. Huh7.5.1-Cas9 (with bicistronic *ACE2*-IRES-*TMPRSS2* construct for SARS-
513 CoV-2 and without for 229E and OC43 screen) were mutagenized using a genome-wide
514 single-guide RNA (sgRNA) library. Mutant cells were infected with each coronavirus
515 separately and virus-resistant cells were harvested 10-14 days post infection (dpi). The
516 abundance of each sgRNA in the starting and selected population was determined by
517 high-throughput sequencing and a gene enrichment analysis was performed.

518 **(B)** Gene enrichment for CRISPR screen of SARS-CoV-2 infection. Enrichment scores
519 were determined by MaGECK analysis and genes were colored by biological function.
520 Dotted line indicates $-\log_{10}(\text{Enrichment Score})=4$. The SARS-CoV-2 was performed
521 once.

522 **(C)** Gene enrichment for CRISPR screen of 229E infection. The 229E screen was
523 performed twice and combined MaGECK scores are displayed.

524 **(D)** Gene enrichment for CRISPR screen of OC43 infection. The OC43 screen was
525 performed twice and combined MaGECK scores are displayed.

526

527 **Figure 2: Gene ontology analysis and network propagation highlight pathways**
528 **and biological networks important for coronavirus infection.**

529 **(A)** Gene ontology (GO) enrichment analysis was performed on significant hits from the
530 individual CRISPR screens (MaGECK enrichment score ≤ 0.005). P values were

531 calculated by hypergeometric test and a false-discovery rate was used to account for
532 multiple hypothesis testing. The top GO terms of each screen were selected for
533 visualization. A complete list of significant GO terms can be found in Table S2.

534 **(B)** Data integration pipeline for network propagation of identified host factor genes.
535 Unthresholded CRISPR screen enrichment scores served as initial gene labels for
536 network propagation using Pathway Commons. Separately propagated networks were
537 integrated gene-wise (via multiplication) to identify biological networks that are shared
538 between all three datasets. Genes found to be significant in the propagation were
539 extracted, clustered into smaller subnetworks, and annotated using GO enrichment
540 analysis (see Methods).

541 **(C)** Selected biological subnetwork clusters from network propagation. Cluster title
542 indicates the most significant biological function(s) for each cluster. Circle size
543 represents p-value from network propagation permutation test (see STAR Methods and
544 Table S3). The original enrichment score of a gene in each CRISPR screen is indicated
545 by color scale within the circle. The entire set of identified clusters is displayed in Figure
546 S3A. (#) is the cluster number, which refers to the GO enrichment analysis of biological
547 processes in Figure S3B and Table S2.

548

549 **Figure 3: Knockout of candidate host factor genes reduces coronavirus infection.**

550 **(A)** RT-qPCR quantification of intracellular SARS-CoV-2 levels in RNP-edited A549-
551 ACE2 cells. A non-targeting sgRNA was used as control. Cells were infected using
552 $\text{moi}=0.1$ and harvested at 72 hours post-infection (hpi).

553 **(B)** RT-qPCR quantification of intracellular SARS-CoV-2 levels in Calu-3 cells lentivirally
554 transduced with Cas9/sgRNA cassettes targeting the indicated genes. A non-targeting
555 sgRNA was used as control. Cells were infected using moi=0.1 and harvested at 48 hpi.

556 **(C)** RT-qPCR quantification of intracellular SARS-CoV-2 levels in WT Huh7.5.1,
557 *TMEM106B* KO or *TMEM106B* KO cells with *TMEM106B* cDNA add-back (AB). Cells
558 were infected using moi=0.1 and harvested at 24 hpi.

559 **(D)** RT-qPCR quantification of intracellular SARS-CoV-2 levels in WT Huh7.5.1, *VAC14*
560 KO or *VAC14* KO cells with *VAC14* cDNA AB. Cells were infected using moi=0.1 and
561 harvested at 24 hpi.

562 **(E)** RT-qPCR quantification of intracellular SARS-CoV-2 levels in WT Huh7.5.1, *SCAP*
563 KO, *MBTPS2* KO or *EXOC2* KO cells. Cells were infected using moi=0.1 and harvested
564 at 24 hpi.

565 **(F)** RT-qPCR quantification of intracellular OC43 and 229E RNA levels in WT and
566 *TMEM106B*, *VAC14*, *SCAP*, *MBTPS2* or *EXOC2* KO Huh7.5.1 cells. Cells were
567 infected using moi=0.05 (229E) and moi=3 (OC43) and harvested at 48 hpi.

568 **(G-I)** RT-qPCR quantification of intracellular viral RNA for **(G)** OC43, **(H)** 229E, or **(I)**
569 SARS-CoV-2 in WT Huh7.5.1 cells or cell lines deficient in *CCZ1B*, *RAB7A*, *VPS16*,
570 *BECN1*, *PIK3R4* or *UVRAG*.

571 **(J-L)** RT-qPCR quantification of intracellular viral RNA for **(J)** SARS-CoV-2, **(K)** OC43,
572 or **(L)** 229E in WT, *PIK3R4* KO or *PIK3R4* KO cells with *PIK3R4* cDNA AB.

573 **(M-O)** RT-qPCR quantification of intracellular viral RNA for **(M)** SARS-CoV-2, **(N)** OC43,
574 or **(O)** 229E in WT, *VPS16* KO or *VPS16* KO cells with *VPS16* cDNA AB.

575 For SARS-CoV-2 infection, viral N gene transcripts were normalized to cellular RNaseP.
576 For OC43 and 229E experiments, viral RNA was normalized to 18S RNA. For all RT-
577 qPCR experiments, results are displayed relative to infection in WT cells and data
578 represent means \pm s.e.m. from 3 biological samples.

579

580 **Figure 4: Pharmacological inhibition of identified host factors decreases infection**
581 **with SARS-CoV-2 and common cold coronaviruses.**

582 **(A-C)** SAR405 (PI3K inhibitor) dose-response curves for **(A)** SARS-CoV-2, **(B)** 229E
583 and **(C)** OC43 replication in Huh7.5.1 cells and for cell viability of SAR405 treated cells.

584 **(D-F)** PF-429242 (MBTPS1 inhibitor) dose-response curves for **(D)** SARS-CoV-2, **(E)**
585 229E, and **(F)** OC43 replication in Huh7.5.1 cells and for cell viability of PF-429242
586 treated cells.

587 **(G-I)** 25-hydroxycholesterol (25-HC) dose-response curves for **(G)** SARS-CoV-2, **(H)**
588 229E, and **(I)** OC43 replication in Huh7.5.1 cells and for cell viability of 25-HC treated
589 cells.

590 **(J-K)** Bardoxolone (KEAP1-NRF2 activator) dose-response curves for **(J)** SARS-CoV-2,
591 **(K)** 229E, and **(L)** OC43 replication in Huh7.5.1 cells and for cell viability of Bardoxolone
592 treated cells.

593 For all experiments, compounds were added simultaneously with virus. Viral RNA was
594 quantified after 24 hpi (SARS-CoV-2) or 48hpi (229E and OC43) using RT-qPCR.
595 SARS-CoV-2 RNA was normalized to RnaseP, and 229E and OC43 RNA was
596 normalized to 18S RNA. Values represent means \pm s.e.m. relative to untreated cells.
597 Cell viability was assessed in parallel in drug-treated, uninfected cells and is displayed

598 as means \pm s.e.m. relative to DMSO or EtOH treated cells. Non-linear curves were fitted
599 with least squares regression using GraphPad Prism 8 and IC_{50} was determined. All
600 experiments were performed in 3 biological replicates.

601

602 **Figure 5: Cholesterol is required for spike-mediated entry of SARS-CoV-2**

603 **(A)** Western blot of ACE2 and TMEM106B levels from Huh7.5.1-*ACE2/TMPRSS2* cells
604 with non-targeting (NT) or *TMEM106B*-targeting RNPs. Lysates were prepared under
605 non-reducing conditions and TMEM106B appears as dimer. GAPDH was used as
606 loading control. Molecular weight markers are indicated on the left.

607 **(B)** VSV-SARS-CoV-2-S infection of clonal Huh7.5.1-*ACE2/TMPRSS2* cells edited with
608 RNPs targeting the specified genes. A non-targeting (NT) sgRNA was used as control.
609 Cells were harvested at 8hpi and analyzed for GFP+ cells using flow cytometry. Values
610 represent five biological replicates and are displayed as means \pm s.d.

611 **(C)** VSV-SARS-CoV-2-S infection of PF-429242 treated cells. Huh7.5.1-
612 *ACE2/TMPRSS2* cells were pretreated with different concentrations of PF-429242 for
613 2h and then infected with virus. Cells were analyzed by flow cytometry at 14hpi and
614 analyzed for GFP+ cells using flow cytometry. Values represent two biological replicates
615 at each concentration and are displayed as means \pm s.d.

616 **(D)** VSV-SARS-CoV-2-S infection of 25-HC treated cells. Huh7.5.1-*ACE2/TMPRSS2*
617 cells were pretreated with different concentrations of 25-HC for 2h and then infected
618 with virus. Cells were analyzed by flow cytometry at 14hpi. Values represent two
619 biological replicates at each concentration and are displayed as means \pm s.d.

620 **SUPPLEMENTAL FIGURE TITLES AND LEGENDS**

621 **Figure S1: Optimization of phenotypic selection of coronavirus infected Huh7.5.1**
622 **cells and quality control metrics for CRISPR screens, Related to Figure 1.**

623 **(A)** Light microscopy images of WT Huh7.5.1 infected with OC43 (7 dpi) and 229E (4
624 dpi). **(B)** Quantification of SARS-CoV-2 RNA in WT Huh7.5.1 cells at 24 and 72 hpi by
625 RT-qPCR. Cq values represent mean \pm s.e.m. from 3 biological replicates.

626 **(C)** Light microscopy images of SARS-CoV-2 infected WT Huh7.5.1 cells or Huh7.5.1
627 cells expressing *ACE2-IRES-TMPRSS2* at 3 and 7 dpi.

628 **(D)** Quantification of ACE2 and TMPRSS2 expression in WT and lentivirally transduced
629 Huh7.5.1 cells by RT-qPCR and Western blot. mRNA levels are displayed as mean \pm
630 s.e.m. from two independent sample collections and are relative to expression in WT
631 cells. Anti-ACE2 and anti-TMPRSS2 antibodies were used to detect protein levels in
632 WT and overexpression cells. GAPDH was used as loading control. Molecular weight
633 markers are indicated on the left.

634 **(E)** Quantification of infection with pseudotyped lentivirus bearing SARS-CoV-2 spike
635 and expressing GFP by flow cytometry. Values are from two biological samples and are
636 displayed as means \pm s.d.

637 **(F)** Quantification of cell survival by measuring cell number of mock or SARS-CoV-2
638 infected Huh7.5.1-*ACE2-IRES-TMPRSS2* cells (moi=0.01) at 3dpi. Values are from two
639 independent wells and are displayed as means \pm s.d.

640 **(G)** sgRNA representation and distribution in the genome-wide CRISPR KO libraries at
641 day 7 post-transduction (prior to coronavirus infection). Reads for each sgRNA were
642 normalized to the total number of reads.

643 **(H)** Gene-level log fold changes (LFCs) between the lentiviral CRISPR library
644 transduced into target cells at day 0 and the KO library cell population at day 7 post-
645 transduction (x-axis) versus gene-level LFCs between the KO library cell population at
646 day 7 post-transduction (prior to virus infection) and after phenotypic selection by
647 coronavirus infection (y-axis). Gene knockouts showing growth defects in absence of
648 virus challenge are highlighted in red.

649 **(I)** LFCs for the individual sgRNAs for the top 10 scoring genes from each CRISPR
650 screen between the starting cell populations and the virus-selected cell populations.
651 Overall sgRNA distribution is shown at the bottom of the graph and dotted line indicates
652 mean LFC of all sgRNAs.

653

654 **Figure S2: Comparison of CRISPR screens reveals common and distinct host**
655 **factors across SARS-CoV-2, 229E and OC43, Related to Figure 1.**

656 **(A)** CRISPR screen ranking of genes (according to MaGECK enrichment scores in
657 Table S1) clustered in specific cellular pathway or complexes across the three CRISPR
658 screens.

659 **(B)** Pairwise comparisons of gene enrichments between CRISPR screens. Dotted lines
660 indicate $-\log_{10}(\text{Enrichment score}) = 3$. Genes that scored above the threshold in both
661 screens are highlighted in red.

662 **(C)** Representation of the 332 high-confidence SARS-CoV-2 protein-protein interactome
663 hits from (Gordon et al., 2020a) (highlighted in red) within the ranked CRISPR screen
664 data for SARS-CoV-2, OC43 and 229E infection. Gene labels are added for interactome
665 hits that scored in the top 500 of the CRISPR screens.

666

667 **Figure S3: Network propagation of CRISPR screen hits reveals functional clusters**
668 **with distinct biological functions, Related to Figure 2.**

669 **(A)** Biological subclusters from network propagation. Cluster number refers to the
670 enrichment analysis of biological processes for each cluster, displayed in Figure S3B.
671 Circle size represents p-value from integrative network propagation permutation test
672 (see Methods and Table S3). The CRISPR screen enrichment score of a gene from
673 each screen is indicated by color scale within the circle.

674 **(B)** Gene ontology (GO) enrichment analysis was performed on each subcluster from
675 the network propagation. P values were calculated by hypergeometric test and a false-
676 discovery rate was used to account for multiple hypothesis testing. The entire set of
677 enriched biological processes for each subcluster is listed in Table S2.

678

679 **Figure S4: Characterization of gene-edited cells, Related to Figure 3.**

680 **(A)** Genotyping of clonal Huh7.5.1. Targeted loci were PCR-amplified, Sanger-
681 sequenced and aligned to WT reference sequence. Frameshifts are highlighted in blue.

682 **(B)** Western blot analysis of WT, KO and KO cells with respective cDNA add-backs
683 (AB) for TMEM106B, VAC14 and PIK3R4. Lysates to probe for TMEM106B were
684 prepared under non-reducing conditions and bands appear as dimers. GAPDH was
685 used as loading control.

686 **(C)** Cell viability measurement of 229E infected WT and KO Huh7.5.1 cells. Cells were
687 infected with 229E (moi=0.05) and viability was determined 8 dpi using Cell Titer Glo.
688 Values are displayed as means \pm s.d. from three biological samples.

689 **(D)** Cell viability measurement of OC43 infected WT and KO Huh7.5.1 cells. Cells were
690 infected with OC43 (moi=3) and viability was determined 8 dpi using Cell Titer Glo.
691 Values are displayed as means \pm s.d. from two biological samples.

692 **(E)** Analysis of cell proliferation of RNP-edited A549-ACE2 cells. Cells were plated in
693 96-wells and confluency was measured daily using an automated microscope. Values
694 are displayed as means \pm s.d. from four separate wells per cell line.

695 **(F)** Analysis of cell proliferation of WT and clonal KO Huh7.5.1 cells. Cells were plated
696 in 96-wells and cell proliferation was measured daily using Cell Titer Glo. Values are
697 displayed as means \pm s.d. from three separate wells per cell line per timepoint.

698

699 **Figure S5: Pharmacological inhibition of host factors in Huh7.5.1 and Calu-3 cells,**
700 **and validation of on-target activity of SREBP pathway inhibitors, Related to**
701 **Figure 4.**

702 **(A-B)** Dose-response curves of the effect of **(A)** YM201636 and **(B)** Fatostatin on
703 SARS-CoV-2 replication in Huh7.5.1 cells and on cell viability of drug treated cells. Viral
704 RNA was quantified after 24 hpi using RT-qPCR and normalized to RnaseP. Values
705 represent means \pm s.e.m. relative to DMSO treated cells. Non-linear curves were fitted
706 with least squares regression using GraphPad Prism 8 and IC_{50} was determined. All
707 experiments were performed with 3 biological replicates.

708 **(C)** Gene expression analysis of the SREBP-regulated cholesterol biosynthesis genes
709 3-Hydroxy-3-Methylglutaryl-CoA Synthase 1 (HMGCS1) and HMG-CoA reductase
710 (HMGCR) as well as SREBP2, LDLR and SCAP in uninfected/no drug, infected/no drug
711 and infected/drug-treated conditions (25 μ M PF-429242 and 6.25 μ M 25-HC) in

712 Huh7.5.1 cells at 24h post-infection/treatment. mRNA levels are displayed as mean \pm
713 s.e.m. from three biological replicates and are relative to expression in uninfected/no
714 drug cells.

715 **(D)** RT-qPCR quantification of intracellular SARS-CoV-2 levels in drug-treated Calu-3
716 cells. Cells were infected using moi=0.1, treated with 5 μ M at time of infection and
717 harvested at 24 hpi. Values represent means \pm s.e.m. from three biological replicates
718 and are relative to the no drug (DMSO treated) condition.

719 **(E)** Cell viability of drug-treated Calu-3 cells 24h after addition of compounds using Cell
720 Titer Glo. Values are displayed as means \pm s.d. from three biological replicates.

721

722 STAR METHODS**723 Resource Availability****724 Lead Contact**

725 Further information and requests for resources and reagents should be directed to and
726 will be fulfilled by the Lead Contact, Andreas S. Puschnik
727 (andreas.puschnik@czbiohub.org).

728

729 Materials Availability

730 All requests for resources and reagents should be directed to and will be fulfilled by the
731 Lead Contact author. Materials will be made available through the authors upon
732 execution of a Material Transfer Agreement.

733

734 Data and Code Availability

735 Raw sequencing data for CRISPR KO screens is deposited on EMBL-EBI ArrayExpress
736 (<https://www.ebi.ac.uk/arrayexpress/>) under the accession number E-MTAB-9638.

737 Additional Supplemental Items are available from Mendeley Data at

738 <http://dx.doi.org/10.17632/r49yg49ddc>.

739

740 Experimental Model and Subject Details**741 Cell lines**

742 Huh7.5.1 (gift from Frank Chisari) (Zhong et al., 2005), HEK293FT (Thermo Scientific),
743 Vero cells (ATCC), VeroE6 (ATCC) and A549-ACE2 cells (gift from Olivier Schwartz)
744 were cultured in DMEM (Gibco) supplemented with 10% fetal bovine serum (FBS,

745 Omega Scientific), penicillin/streptomycin (Gibco), non-essential amino acids (Gibco)
746 and L-glutamine (Gibco) at 37C and 5% CO₂. Calu-3 cells (ATCC) were cultured in
747 DMEM/F12 (Gibco) supplemented with 10% FBS (Omega Scientific),
748 penicillin/streptomycin (Gibco), non-essential amino acids (Gibco) and L-glutamine
749 (Gibco) at 37C and 5% CO₂. Huh7.5.1 and 293FT cell lines were tested negative for
750 mycoplasma contamination.

751

752 **Virus stocks**

753 OC43 was obtained from ATCC (VR-1558) and propagated in Huh7.5.1 cells at 33C.
754 229E was obtained from ATCC (VR-740) and propagated in Huh7.5.1 cells at 33C.
755 SARS-CoV-2 (USA/WA-1/2020 strain) was obtained through BEI Resources (NR-
756 52281) and propagated in Vero cells at 37C. Supernatants were collected when
757 cytopathic effect was apparent, filtered and stored at -80C. Viral titers were determined
758 by standard plaque assay using either Huh7.5.1 cells (OC43 and 229E) or Vero cells
759 (SARS-CoV-2). Briefly, serial 10-fold dilutions of virus stocks were used to infect cells in
760 6-well plates for 1h and an overlay of DMEM media containing 1.2% Avicel RC-591 was
761 added. Cells were incubated for 3-4 days, followed by fixation with 10% formaldehyde,
762 staining with crystal violet and plaque counting. Additionally, SARS-CoV-2 stock was
763 sequence-verified by next-generation sequencing. All experiments with OC43 and 229E
764 were performed in a biosafety level 2 laboratory and all experiments involving SARS-
765 CoV-2 were performed in a biosafety level 3 laboratory.

766

767 **Method Details**

768 Plasmids, cloning and lentivirus production

769 The following cDNA sequence containing plasmids were obtained: *hACE2* (Addgene,
770 #1786, gift from Hyeryun Choe) (Li et al., 2003), *TMPRSS2* (Addgene, #53887, gift from
771 Roger Reeves) (Edie et al., 2018), *TMEM106B* (Genscript, OHu17671), *VAC14*
772 (Addgene, #47418, gift from Peter McPherson) (Lemaire and McPherson, 2006),
773 *PIK3R4* (Addgene, #23488, gift from William Hahn & David Root) (Johannessen et al.,
774 2010) and *VPS16* (Addgene, #67023, gift from Noboru Mizushima) (Jiang et al., 2014).

775 Individual cDNAs were cloned into EcoRV-cut plenti-CMV-Puro-DEST (Addgene,
776 #17452, gift from Eric Campeau & Paul Kaufman) (Campeau et al., 2009) (*TMEM106B*,
777 *VAC14*, *PIK3R4*, *VPS16*) or plenti-CMV-Hygro-DEST (Addgene, #17454, gift from Eric
778 Campeau & Paul Kaufman) (Campeau et al., 2009) (*hACE2*, *TMPRSS2*) using
779 NEBuilder HiFi DNA Assembly Master Mix (NEB). To generate the plenti-CMV-*ACE2*-
780 IRES-*TMPRSS2* construct, *ACE2*, EMCV IRES (derived from pLenti-
781 DsRed_IRES_EGFP (Addgene, #92194, gift from Huda Zoghbi)) (Rousseaux et al.,
782 2016), and *TMPRSS2* were individually amplified with addition of overlapping
783 sequences and the three fragments were assembled using NEBuilder HiFi DNA
784 Assembly Master Mix. To generate plenti-*TMPRSS2*-TwinStrep, *TMPRSS2* was
785 inserted into a plenti-CMV-GFP-Zeo vector (Addgene, # 17449, gift from Eric Campeau
786 & Paul Kaufman) (Campeau et al., 2009) via digestion with BamHI and Sall followed by
787 assembly using the Gibson Assembly master mix (NEB). All primer sequences for
788 cloning can be found in Table S5.

789 Lentivirus was produced in HEK293FT by co-transfection of cDNA containing lentiviral
790 plasmid together with pCMV-dR8.2 dvpr (Addgene, #8455, gift from Bob Weinberg)

791 (Stewart et al., 2003), pCMV-VSV-G (Addgene, #8454, gift from Bob Weinberg)
792 (Stewart et al., 2003) and pAdVantage (Promega) using FugeneHD (Promega).
793 Supernatants were collected 48h post-transfection, filtered and added to recipient cells
794 in presence of Polybrene (SCBT). Transduced cells were subsequently selected using
795 Puromycin or Hygromycin for 5-7 days.

796

797 **Genome-wide CRISPR screens**

798 Huh7.5.1-Cas9 cells were generated by lentiviral transduction with lentiCas9-blast
799 (Addgene, #52962, gift from Feng Zhang) (Sanjana et al., 2014) and subsequently
800 selected with blasticidin for 7 days. A portion of Huh7.5.1-Cas9 cells were additionally
801 transduced with lentivirus containing *ACE2-IRES-TMPRSS2-hygro*. To generate
802 CRISPR KO libraries, a total of 240 million Huh7.5.1-Cas9-blast or Huh7.5.1-Cas9-
803 blast+*ACE2-IRES-TMPRSS2-hygro* cells were transduced with lentivirus of the human
804 GeCKO v2 library (Addgene, #1000000049, gift from Feng Zhang) (Sanjana et al.,
805 2014) at a moi of 0.4 and subsequently selected using puromycin and expanded for 7
806 days. A total of 60 million mutagenized cells for each GeCKO sublibrary (A and B) were
807 collected for genomic DNA extraction to assess the sgRNA representation of the
808 starting population at day 7 post-transduction. In order to assess the sgRNA
809 representation in the lentiviral supernatant used for transduction at day 0, we isolated
810 lentiviral genomes using the DirectZol kit (Zymo), reverse-transcribed the purified RNA
811 and amplified the sgRNA sequences as described below.

812 For the SARS-CoV-2 CRISPR host factor screen, 100 million cells of Huh7.5.1-Cas9-
813 blast+*ACE2-IRES-TMPRSS2-hygro* GeCKO library cells were infected with SARS-CoV-

814 2 at a multiplicity of infection (moi) of 0.01. Virus-induced cell death was apparent after
815 2-3 days and surviving cells were collected 12 dpi. The screen was performed once.
816 For the 229E and OC43 CRISPR screens, 100 million cells (per screen) of Huh7.5.1-
817 Cas9-blast GeCKO library cells were infected with 229E and OC43 at moi of 0.05 and 3,
818 respectively. Cells were incubated at 33C to increase CPE, which was apparent after 3-
819 4 days. Surviving cells were collected after 10 days for 229E and 14 days for OC43.
820 Each screen was performed in two replicates. For all CRISPR screens, genomic DNA
821 (gDNA) was extracted using either QIAamp DNA Blood Maxi Kit (Qiagen) or Quick-DNA
822 Midiprep Plus (Zymo). The sgRNA expression cassettes were amplified from gDNA in a
823 two-step nested PCR using KAPA HiFi HotStart ReadyMixPCR Kit (Kapa Biosystems).
824 For PCR1, 40 reactions (for control samples) and 10-16 reactions (for virus selected
825 samples) containing 4 µg gDNA were set up and amplified for 16 cycles. Reactions
826 were pooled, mixed and 200 µl were cleaned up using QIAquick PCR Purification kit
827 (Qiagen). For PCR2, 3 reactions containing 5 µl PCR1 product were amplified for 12
828 cycles using indexed primers. PCR products were gel purified using QIAquick Gel
829 Extraction Kit (Qiagen) and sequenced on an Illumina NextSeq 500 using a custom
830 sequencing primer. Primers sequences are listed in Table S5.
831 Demultiplexed FASTQ files were aligned to a reference table containing sgRNA
832 sequences and abundance of each sgRNA was determined for each starting and
833 selected cell population. Guide count tables were further processed using MaGECK
834 with default "norm-method" to determine positive enrichment scores for each gene (Li et
835 al., 2014). For 229E and OC43, two biological screen replicates were used as input, and
836 for SARS-CoV-2, one biological screen replicate was used. The gene ontology

837 enrichment of the individual screens was run on genes with MaGECK positive score \leq
838 0.005 using the GO Biological Processes of the Molecular Signatures Database
839 (MSigDB).

840

841 **Network propagation**

842 We performed network propagation analysis for the three virus CRISPR screens using
843 the Pathway Commons network (Cerami et al., 2011). Specifically, we used a heat-
844 diffusion kernel analogous to random walk with restart (RWR, also known as insulated
845 diffusion and personalized PageRank) which better captures the local topology of the
846 interaction network compared to a general heat diffusion process. The process is
847 captured by the steady-state solution as follows:

$$848 \quad P_{SS} = \alpha(I - (1 - \alpha)W)^{-1}P_0$$

849 where P_{SS} represents the vector of propagated values at steady-state, P_0 is the initial
850 labeling (genes of interest from molecular studies), W is the normalized version of the
851 adjacency matrix of the underlying network (in this implementation $W = AD^{-1}$, where A
852 is the unnormalized adjacency matrix, and D is the diagonal degree matrix of the
853 network), I is the identity matrix, and α denotes the restart probability (here, $\alpha=0.2$),
854 which is the probability of returning to the previously visited node, thus controlling the
855 spread through the network.

856 We performed three independent propagations, one for each CRISPR dataset (i.e. each
857 virus). After propagation, each propagated network was integrated by multiplying gene-
858 wise. Such an operation is used to create a gene list ranked to prioritize genes with high
859 scores from all propagated datasets. To control for nodes with high degree (i.e. many

860 connections), which due to their heightened connectivity are biased to receive higher
861 propagation scores, we conducted a permutation test. Specifically, we simulated
862 random propagations by shuffling the positive scores to random genes, repeating this
863 20,000 times per CRISPR screen. Next, we calculated an empirical p-value by
864 calculating the fraction of random propagation runs greater than or equal to the true
865 propagation run for each gene.

866 The network was created by extracting a subnetwork from the same Pathway Commons
867 network corresponding to genes possessing a significant p-value ($p \leq 0.01$) from the
868 propagation ($n=378$). Of these, interconnected genes were visualized using Cytoscape
869 ($n=284$). The resulting network was clustered into subnetworks using the GLay
870 Cytoscape plugin (Su et al., 2010). Three large clusters (1, 3, and 5) were further
871 clustered using GLay into additional subclusters (denoted with letters), resulting in a
872 total of 25 subnetwork clusters (see Figure S3A and Table S3). Lastly, Gene Ontology
873 (GO) enrichment analysis (biological process) was performed for each of the 25
874 resulting subclusters to identify biological processes and pathways associated with each
875 subcluster.

876

877 **Generation of clonal Huh7.5.1 KO cell lines**

878 sgRNA sequences against gene targets were designed using the GPP sgRNA Designer
879 (<https://portals.broadinstitute.org/gpp/public/analysis-tools/sgrna-design>). DNA oligos
880 (IDT) containing sgRNA sequences were annealed and ligated into pX458 (Addgene,
881 #48138, gift from Feng Zhang) (Ran et al., 2013). Cells were transfected with pX458
882 constructs using Mirus TransIT-X2 (Mirus Bio) and two days later GFP positive cells

883 were single-cell sorted into 96-well plates using a Sony SH800 cell sorter. For
884 genotyping, genomic DNA was isolated from obtained clones using DNA QuickExtract
885 (Lucigen), the sgRNA-targeted sites PCR amplified and the products Sanger-
886 sequenced. Obtained sequences were compared to reference sequences and clones
887 containing a frameshift indel or de novo stop codon were selected. A list of all used
888 sgRNA sequences and genotyping primers can be found in Table S5.

889 To isolate a clonal Huh7.5.1-ACE2/TMPRSS2 cell line, polyclonal Huh7.5.1-
890 ACE2/TMPRSS2 were diluted and plated in 96-well plates. Single colonies were grown
891 up and clones were screened for high expression of ACE2 and TMPRSS2 by Western
892 blot.

893

894 **Generation of RNP edited A549-ACE2 and Huh7.5.1-ACE2/TMPRSS2 cells**

895 sgRNAs were designed according to Synthego's multi-guide gene knockout. Briefly, two
896 or three sgRNAs are bioinformatically designed to work in a cooperative manner to
897 generate small, knockout-causing, fragment deletions in early exons. These fragment
898 deletions are larger than standard indels generated from single guides. The genomic
899 repair patterns from a multi-guide approach are highly predictable based on the guide-
900 spacing and design constraints to limit off-targets, resulting in a higher probability
901 protein knockout phenotype.

902 RNA oligonucleotides were chemically synthesized on Synthego solid-phase synthesis
903 platform, using CPG solid support containing a universal linker. 5-Benzylthio-1H-
904 tetrazole (BTT, 0.25 M solution in acetonitrile) was used for coupling, (3-
905 ((Dimethylamino-methylidene)amino)-3H-1,2,4-dithiazole-3-thione (DDTT, 0.1 M

906 solution in pyridine) was used for thiolation, dichloroacetic acid (DCA, 3% solution in
907 toluene) for used for detritylation. Modified sgRNA were chemically synthesized to
908 contain 2'-O-methyl analogs and 3' phosphorothioate nucleotide interlinkages in the
909 terminal three nucleotides at both 5' and 3' ends of the RNA molecule. After synthesis,
910 oligonucleotides were subject to series of deprotection steps, followed by purification by
911 solid phase extraction (SPE). Purified oligonucleotides were analyzed by ESI-MS.

912 To induce gene knockout in A549-ACE2 cells, 5 pmol *Streptococcus Pyogenes* NLS-
913 Sp.Cas9-NLS (SpCas9) nuclease (Aldevron) was combined with 15 pmol total synthetic
914 sgRNA (5 pmol each sgRNA) (Synthego) to form ribonucleoproteins (RNPs) in 20uL
915 total volume with SE Buffer (Lonza). To induce knockouts in Huh7.5.1-ACE2/TMPRSS2
916 cells, 30 pmol total synthetic sgRNA was mixed with 10 pmol Cas9 in 20uL total volume
917 SE buffer. The RNP assembly reaction was mixed by pipetting up and down and
918 incubated at room temperature for 10 minutes.

919 All cells were dissociated into single cells using TrypLE Express (Gibco), as described
920 above, resuspended in culture media and counted. For A549-ACE2 transfections,
921 100,000 cells per reaction were used while for Huh7.5.1-ACE2/TMPRSS2 200,000 cells
922 per reaction were used. Cells were pelleted by centrifugation at 200 xg for 5 minutes.
923 Following centrifugation, cells were resuspended in transfection buffer according to cell
924 type. 5 μ L of cell solution was added to preformed RNP solution and gently mixed.
925 Nucleofections were performed on a Lonza HT 96-well nucleofector system using
926 program CM-120 and CM-104 for A549-ACE2 and Huh7.5.1-ACE2/TMPRSS2,
927 respectively. All transfections were performed in Lonza SE buffer. Immediately following
928 nucleofection, each reaction was divided evenly between two wells of a tissue-culture

929 treated 96-well plate containing 100 μ L normal culture media. Two days post-
930 nucleofection, DNA was extracted from using DNA QuickExtract (Lucigen). Amplicons
931 for indel analysis were generated by PCR amplification. PCR products were cleaned-up
932 and analyzed by sanger sequencing. Sanger data files and sgRNA target sequences
933 were input into Inference of CRISPR Edits (ICE) analysis (ice.synthego.com) to
934 determine editing efficiency and to quantify generated indels (Hsiao et al., 2019). A list
935 of all used sgRNA sequences and genotyping primers can be found in Table S5.

936

937 **Generation of polyclonal Calu-3 KO cell lines**

938 DNA oligos (IDT) containing sgRNA sequences (see Table S5) were annealed and
939 ligated into lentiCRISPRv2 (Addgene, #52961, gift from Feng Zhang) (Sanjana et al.,
940 2014). Lentivirus for each individual construct was produced as described above. Calu-
941 3 cells were co-transduced with two lentiviruses encoding separate sgRNAs per gene or
942 with a non-targeting sgRNA encoding lentivirus in presence of polybrene. Transduced
943 Calu-3 cells were selected with puromycin (2 μ g/ml) for 9 days prior to infection
944 experiments.

945

946 **RT-qPCR infection assays**

947 Cells were plated in 96-well plates and infected the next day with virus: OC43 (moi=3),
948 229E (moi=0.05), SARS-CoV-2 (moi=0.1). For infection with HCoVs, cells were
949 harvested 48 hpi, lysates were reverse transcribed and quantitative PCR was performed
950 on a Bio-Rad CFX96 Touch system using the Power SYBR Cells-to-CT kit (Invitrogen)
951 according to the manufacturer's instructions. 229E and OC43 RNA levels were

952 quantified with virus-specific primer sets and viral RNA levels were normalized to
953 cellular 18S levels.

954 For SARS-CoV-2 infections, Huh7.5.1, Calu-3 and A549-ACE2 cells were harvested
955 after 24, 48 and 72h, respectively, using 200 μ l DNA/RNA Shield (Zymo) to inactivate
956 virus prior to export from the BSL3 laboratory. Samples were extracted using the Quick-
957 DNA/RNA Viral MagBead kit (Zymo) on a Bravo automated liquid handling platform
958 (Agilent). Briefly, the Bravo RNA extraction protocol consists of: 1) 180 μ l sample
959 transfer from 2mL deep well to a 1mL deep well plate containing Proteinase K; 2)
960 addition of Zymo Viral DNA/RNA Buffer for sample lysis; 3) Addition of Zymo
961 MagBeads; 4) 10 minute mixing and shaking of samples with lysis buffer and
962 MagBeads; 5) incubation of the mixture on a 96 well ring magnet to collect the beads to
963 a ring at the bottom of the deep well plate; 6) aspiration of the supernatant and
964 dispensing into a 2mL deep well waste plate; 7) addition of wash buffers 1 with mixing;
965 8) incubation on the 96 well ring magnet; 9) aspiration. Steps 7-9 are repeated for wash
966 buffer 2 and two rounds of 100% ethanol. 10) incubation on the magnet for 20 minutes
967 to fully evaporate residual 100% ethanol from the beads; 11) Elution with nuclease-free
968 water.

969 For RT-qPCR, separate reactions were performed for the quantification of SARS-CoV-2
970 N and E gene transcripts as well as cellular RNaseP for normalization using the Luna
971 Universal Probe One-Step RT-qPCR Kit (NEB) on a Bio-Rad CFX384 Touch system. N
972 and E gene transcripts showed high concordance and N gene levels normalized to
973 RNaseP were displayed in figures. All qPCR primer/probe sequences are listed in Table
974 S5.

975

976 Western blots

977 Cells were lysed using Laemmli SDS sample buffer containing 5% beta-
978 mercaptoethanol and boiled at 95C for 10min with the exception of lysates for
979 TMEM106B immunoblotting. In this case, cells were lysed in RIPA buffer on ice for
980 15min, then mixed with Laemmli under non-reducing conditions and without boiling. All
981 lysates were separated by SDS-PAGE on pre-cast Bio-Rad 4-15% poly-acrylamide gels
982 in Bio-Rad Mini-Protean electrophoresis system. Proteins were transferred onto PVDF
983 membranes using Bio-Rad Trans-Blot Turbo transfer system. PVDF membranes were
984 blocked with PBS buffer containing 0.1% Tween-20 and 5% non-fat milk. Blocked
985 membranes were incubated with primary antibody diluted in blocking buffer and
986 incubated overnight at 4C on a shaker. Primary antibodies were detected by incubating
987 membranes with 1:5000 dilution of HRP-conjugated (Southern Biotech) secondary anti-
988 mouse and anti-rabbit antibodies for 1 h at room temperature. Blots were visualized
989 using a ChemiDoc MP Imaging System (Bio-Rad). The following primary antibodies and
990 their dilutions were used in this study: GAPDH (SCBT, sc-32233) at 1:2000, ACE2
991 (R&D Systems, AF933) at 1:1000, TMPRSS2 (Abcam, ab92323) at 1:1000, TMEM106B
992 (Sigma, HPA058342) at 1:2500, VAC14 (SCBT, sc-271831) at 1:2500, PIK3R4 (Novus
993 Biologicals, NBP1-30463) at 1:2500.

994

995 Lentiviral pseudo-typed virus infection

996 Cells were plated in 96-well plates and infected with 30 μ l of SARS-CoV-2 Reporter
997 Virus Particles (Integral Molecular, RVP-701) per well. After 48-72h, infection rates were

998 measured according the GFP levels using a Cytoflex flow cytometer (Beckman Coulter
999 Life Sciences).

1000

1001 **Generation of SARS-CoV-2-S pseudotyped Vesicular stomatitis virus (VSV-SARS-**
1002 **CoV-2-S)**

1003 SARS-2-S (based on Wuhan-Hu-1 isolate, GenBank: MN908947.3) was generated
1004 using codon optimized gBlock fragments (IDT) spanning genome fragments from
1005 18851-19820, 19771-20740, 20692-21595, 21544-22338, and 22289-22745 (see Table
1006 S5), assembled by Gibson Assembly. Two mutation (K1269A and H1271A) to remove a
1007 prospective ER retention domain) based on data from SARS-CoV1 (McBride et al.,
1008 2007) were introduced by PCR. This gene was assembled into VSV-eGFP-dG
1009 (Addgene, #31842, gift from Connie Cepko) (Beier et al., 2011) in frame with the G
1010 coding sequence between MluI and NotI to generate VSV-eGFP-CoV2-S(AA). Helper
1011 plasmids for rescue were generated by amplification of genes from VSV-eGFP-dG and
1012 cloning by restriction digestion and ligation into pCAGEN (Addgene, # 11160, gift from
1013 Connie Cepko) (Matsuda and Cepko, 2004) to generate pCAGEN-VSV-N, pCAGEN-
1014 VSV-P, and pCAGEN-VSV-L. To rescue the VSVdG-CoV2-S(AA), 293FT cells were co-
1015 cultured with Huh7.5.1 cells at a ratio of 1:2 in a 6-well plate to be 80-90% confluent the
1016 next day. Cells were transfected using JetOptimus (Polyplus) with pCAGGS-T7 (200ng),
1017 pCAGEN-CoV2-N (300ng), pCAGEN-CoV2-P (500ng), pCAGEN-CoV2-L (200ng),
1018 pCMV-VSV-G (800ng), and VSV-eGFP-CoV2-S(AA) (650ng). Cells were trypsinized
1019 and passed to a 10cm plate at 4 days post-transfection. At 10 days post-transfection,
1020 syncytia formation was seen and at 11 days post-transfection most of the cells had

1021 strong green fluorescence and supernatant was collected and frozen at -80°C. Huh7.5.1
1022 cells were infected with supernatant and passaged 6 times every 3-4 days. Passage 6
1023 supernatant was collected and a plaque assay was performed using VeroE6-TMPRSS2
1024 cells. At day 4, plaques were isolated and grown on VeroE6-TMPRSS2- cells. Stock
1025 virus used for experiments was generated by infecting VeroE6 cells at 34°C for 3 days
1026 and collecting supernatant. Clarified supernatant was supplemented with sucrose
1027 phosphate and frozen at -80°C. Viruses were titrated on VeroE6-TMPRSS2 cells. To
1028 sequence the S region of the virus, RNA was isolated using the QiaAmp viral RNA mini
1029 kit (Qiagen). The S regions was amplified using SuperScript III One-Step RT-PCR
1030 System with Platinum Taq DNA Polymerase (Invitrogen). Mutations in S were detected
1031 with a 27nt (9aa) deletion at the C-terminus (1274STOP) and a partial mutation A372T
1032 (~50%) in the ectodomain. Similar adaptive mutations were found in previously
1033 published VSVdG-CoV2-S (Dieterle et al., 2020).

1034

1035 **Flow cytometry analysis of VSV-SARS-CoV-2-S infected cells**

1036 Cells plated in 96-well plates were spin-infected with VSV-SARS-CoV-2-S (800g,
1037 60min, 34C) and subsequently cultured at 37C for 7-14hpi. For analysis of VSV-SARS-
1038 CoV-2-S infection rates, cells were trypsinized, and analyzed using a Cytoflex S flow
1039 cytometer (Beckman Coulter). Approximately 5,000 cells were recorded and gated
1040 based on FSC/SSC, FSC-H/FSC-A (singlets) and FITC (eGFP) using FlowJo 10.

1041

1042 **Compounds**

1043 The following compounds were used in this study: SAR405 (SelleckChem, S7682),
1044 YM201636 (SelleckChem, S1219), PF-429242 dihydrochloride (Sigma, SML0667), 25-
1045 Hydroxycholesterol (Sigma, H1015), Bardoxolone (SelleckChem, S6647) and Fatostatin
1046 HBr (SelleckChem, S8284). 25-Hydroxycholesterol was resuspended in 100% ethanol
1047 and all other compounds were resuspended in DMSO. All compounds were stored at -
1048 20C until use.

1049

1050 **Cell viability and growth assays**

1051 Huh7.5.1 or Calu-3 cells were treated with compounds at the same concentrations and
1052 durations as in infection assays. Cell viability was measured using Cell Titer Glo
1053 (Promega) by mixing cells in 40 μ l media with 40 μ l assay buffer and reading the
1054 luminescence signal on Envision 2105 plate reader (Perkin Elmer). To assess cell
1055 growth for WT and KO Huh7.5.1 cells, cells were plated in 96-well plates and Cell Titer
1056 Glo assay was performed daily for three consecutive days. To assess cell growth for
1057 RNP-edited A549-ACE2 cells, proliferation was determined by confluence of knockout
1058 pools using a Celigo Imaging Cytometer (Celigo) with built in 'Confluence' image
1059 analysis pipeline. Each well was independently imaged using brightfield illumination,
1060 autoexposure and autofocus with a 40 μ m focus offset to increase contrast. Analysis
1061 was performed using standard settings except for an intensity threshold of 8. To
1062 measure the number of surviving cells upon SARS-CoV-2 challenge, cells were plated
1063 in a 96-well black plates with glass bottom and infected with $\text{moi}=0.01$. Cells were fixed
1064 with 4% paraformaldehyde followed by PBS washes. Nuclei were counted after staining
1065 with Hoechst 33258. Images were taken at the Gladstone Institutes Assay Development

1066 and Drug Discovery Core facility on a Molecular Devices ImageXpress confocal
1067 microscope using a 10X objective. Nuclear fluorescence was measured and counted by
1068 MetaXpress software using a multi-wavelength cell scoring module.

1069

1070 **Quantification and Statistical Analysis**

1071 For CRISPR screens, the enrichment scores, p-values and false-discovery rates were
1072 determined using the MaGeCK algorithm (Li et al., 2014). For the GO analysis, p-values
1073 of hypergeometric tests were determined using the Cluster Profiler enricher function in
1074 R and adjusted with “fdr” correction method. For viral infection, drug treatment, and cell
1075 growth experiments biological replicates are defined as independent treatments and
1076 measurements from cells separately plated in and harvested from multiple wells.
1077 Replicates are displayed as mean \pm s.e.m. or mean \pm s.d. as specified in the figure
1078 legends. Mean \pm s.e.m. for RT-qPCR data was determined using CFX Maestro
1079 Software (Bio-Rad) and then visualized in GraphPad Prism 8. Mean \pm s.e.m. or mean \pm
1080 s.d. for remaining data was calculated and visualized using GraphPad Prism 8. Dose-
1081 response curves for drug treatments were generated by applying a non-linear curve fit
1082 with least squares regression and default parameters using GraphPad Prism 8. No
1083 additional statistical tests were performed. No methods were used to determine sample
1084 size estimation or whether the data met assumptions of the statistical approaches. For
1085 all experiments, the statistical details can be found in the figure legends.

1086

1087 **SUPPLEMENTAL TABLES**

1088 **Table S1:** CRISPR screen results. MaGECK output for positive gene enrichment
1089 analysis of SARS-CoV-2, 229E and OC43 host factor screens. Related to Figure 1.

1090 **Table S2:** Gene ontology enrichment analysis of individual CRISPR screens and
1091 network propagation clusters. Related to Figure 2.

1092 **Table S3:** Network propagation results. Related to Figure 2.

1093 **Table S4:** RNP editing efficiencies in A549-ACE2 and Huh7.5.1-ACE2/TMPRSS2 cells.
1094 Related to Figures 3 and 5.

1095 **Table S5:** Oligonucleotide sequences used in this study. Related to STAR Methods.

1096

1097

1098 **REFERENCES**

- 1099 Aoki, T., Ichimura, S., Itoh, A., Kuramoto, M., Shinkawa, T., Isobe, T., and Tagaya, M. (2009).
1100 Identification of the neuroblastoma-amplified gene product as a component of the syntaxin 18
1101 complex implicated in Golgi-to-endoplasmic reticulum retrograde transport. *Mol. Biol. Cell* *20*,
1102 2639–2649.
- 1103 Baggen, J., Persoons, L., Jansen, S., Vanstreels, E., Jacquemyn, M., Jochmans, D., Neyts, J.,
1104 Dallmeier, K., Maes, P., and Daelemans, D. (2020). Identification of TMEM106B as proviral host
1105 factor for SARS-CoV-2. *BioRxiv* 2020.09.28.316281.
- 1106 Balderhaar, H.J. kleine, and Ungermann, C. (2013). CORVET and HOPS tethering complexes –
1107 coordinators of endosome and lysosome fusion. *J. Cell Sci.* *126*, 1307–1316.
- 1108 Beier, K.T., Saunders, A., Oldenburg, I.A., Miyamichi, K., Akhtar, N., Luo, L., Whelan, S.P.J.,
1109 Sabatini, B., and Cepko, C.L. (2011). Anterograde or retrograde transsynaptic labeling of CNS
1110 neurons with vesicular stomatitis virus vectors. *Proc. Natl. Acad. Sci. U. S. A.* *108*, 15414–15419.
- 1111 Bekerman, E., and Einav, S. (2015). Combating emerging viral threats. *Science* *348*, 282–283.
- 1112 Bertram, S., Dijkman, R., Habjan, M., Heurich, A., Gierer, S., Glowacka, I., Welsch, K., Winkler,
1113 M., Schneider, H., Hofmann-Winkler, H., et al. (2013). TMPRSS2 Activates the Human
1114 Coronavirus 229E for Cathepsin-Independent Host Cell Entry and Is Expressed in Viral Target
1115 Cells in the Respiratory Epithelium. *J. Virol.* *87*, 6150–6160.
- 1116 Bilanges, B., Posor, Y., and Vanhaesebroeck, B. (2019). PI3K isoforms in cell signalling and
1117 vesicle trafficking. *Nat. Rev. Mol. Cell Biol.* *20*, 515–534.
- 1118 Bouhaddou, M., Memon, D., Meyer, B., White, K.M., Rezelj, V.V., Correa Marrero, M., Polacco,
1119 B.J., Melnyk, J.E., Ulferts, S., Kaake, R.M., et al. (2020). The Global Phosphorylation Landscape of
1120 SARS-CoV-2 Infection. *Cell*.
- 1121 Brown, M.S., Radhakrishnan, A., and Goldstein, J.L. (2018). Retrospective on Cholesterol
1122 Homeostasis: The Central Role of Scap. *Annu. Rev. Biochem.* *87*, 783–807.
- 1123 Campeau, E., Ruhl, V.E., Rodier, F., Smith, C.L., Rahmberg, B.L., Fuss, J.O., Campisi, J., Yaswen,
1124 P., Cooper, P.K., and Kaufman, P.D. (2009). A versatile viral system for expression and depletion
1125 of proteins in mammalian cells. *PLoS One* *4*, e6529.
- 1126 Carette, J.E., Raaben, M., Wong, A.C., Herbert, A.S., Obernosterer, G., Mulherkar, N., Kuehne,
1127 A.I., Kranzusch, P.J., Griffin, A.M., Ruthel, G., et al. (2011). Ebola virus entry requires the
1128 cholesterol transporter Niemann–Pick C1. *Nature* *477*, 340–343.
- 1129 Cerami, E.G., Gross, B.E., Demir, E., Rodchenkov, I., Babur, Ö., Anwar, N., Schultz, N., Bader,
1130 G.D., and Sander, C. (2011). Pathway Commons, a web resource for biological pathway data.
1131 *Nucleic Acids Res.*

- 1132 Charlton, F.W., Hover, S., Fuller, J., Hewson, R., Fontana, J., Barr, J.N., and Mankouri, J. (2019).
1133 Cellular cholesterol abundance regulates potassium accumulation within endosomes and is an
1134 important determinant in bunyavirus entry. *J. Biol. Chem.* *294*, 7335–7347.
- 1135 Clausen, T.M., Sandoval, D.R., Spliid, C.B., Pihl, J., Perrett, H.R., Painter, C.D., Narayanan, A.,
1136 Majowicz, S.A., Kwong, E.M., McVicar, R.N., et al. (2020). SARS-CoV-2 Infection Depends on
1137 Cellular Heparan Sulfate and ACE2. *Cell* *0*.
- 1138 Cowen, L., Ideker, T., Raphael, B.J., and Sharan, R. (2017). Network propagation: a universal
1139 amplifier of genetic associations. *Nat. Rev. Genet.* *18*, 551–562.
- 1140 Cuadrado, A., Rojo, A.I., Wells, G., Hayes, J.D., Cousin, S.P., Rumsey, W.L., Attucks, O.C.,
1141 Franklin, S., Levonen, A.-L., Kensler, T.W., et al. (2019). Therapeutic targeting of the NRF2 and
1142 KEAP1 partnership in chronic diseases. *Nat. Rev. Drug Discov.* *18*, 295–317.
- 1143 Cuadrado, A., Pajares, M., Benito, C., Jiménez-Villegas, J., Escoll, M., Fernández-Ginés, R., Yagüe,
1144 A.J.G., Lastra, D., Manda, G., Rojo, A.I., et al. (2020). Can Activation of NRF2 Be a Strategy
1145 against COVID-19? *Trends Pharmacol. Sci.* *41*, 598–610.
- 1146 Daniels, L.B., Sitapati, A.M., Zhang, J., Zou, J., Bui, Q.M., Ren, J., Longhurst, C.A., Criqui, M.H.,
1147 and Messer, K. (2020). Relation of Statin Use Prior to Admission to Severity and Recovery
1148 Among COVID-19 Inpatients. *Am. J. Cardiol.* *0*.
- 1149 Daniloski, Z., Jordan, T.X., Wessels, H.-H., Hoagland, D.A., Kasela, S., Legut, M., Maniatis, S.,
1150 Mimitou, E.P., Lu, L., Geller, E., et al. (2020). Identification of Required Host Factors for SARS-
1151 CoV-2 Infection in Human Cells. *Cell*.
- 1152 Dieterle, M.E., Haslwanter, D., Bortz, R.H., Wirchnianski, A.S., Lasso, G., Vergnolle, O., Abbasi,
1153 S.A., Fels, J.M., Laudermilch, E., Florez, C., et al. (2020). A Replication-Competent Vesicular
1154 Stomatitis Virus for Studies of SARS-CoV-2 Spike-Mediated Cell Entry and Its Inhibition. *Cell Host*
1155 *Microbe* *28*, 486-496.e6.
- 1156 Dong, E., Du, H., and Gardner, L. (2020). An interactive web-based dashboard to track COVID-19
1157 in real time. *Lancet Infect. Dis.* *20*, 533–534.
- 1158 Drosten, C., Günther, S., Preiser, W., van der Werf, S., Brodt, H.-R., Becker, S., Rabenau, H.,
1159 Panning, M., Kolesnikova, L., Fouchier, R.A.M., et al. (2003). Identification of a Novel
1160 Coronavirus in Patients with Severe Acute Respiratory Syndrome. *N. Engl. J. Med.* *348*, 1967–
1161 1976.
- 1162 Edie, S., Zaghoul, N.A., Leitch, C.C., Klinedinst, D.K., Lebron, J., Thole, J.F., McCallion, A.S.,
1163 Katsanis, N., and Reeves, R.H. (2018). Survey of Human Chromosome 21 Gene Expression
1164 Effects on Early Development in *Danio rerio*. *G3 Bethesda Md* *8*, 2215–2223.
- 1165 Flint, M., Chatterjee, P., Lin, D.L., McMullan, L.K., Shrivastava-Ranjan, P., Bergeron, É., Lo, M.K.,
1166 Welch, S.R., Nichol, S.T., Tai, A.W., et al. (2019). A genome-wide CRISPR screen identifies N-

- 1167 acetylglucosamine-1-phosphate transferase as a potential antiviral target for Ebola virus. *Nat.*
1168 *Commun.* *10*, 285.
- 1169 Fung, T.S., and Liu, D.X. (2019). Human Coronavirus: Host-Pathogen Interaction. *Annu. Rev.*
1170 *Microbiol.* *73*, 529–557.
- 1171 Gordon, D.E., Jang, G.M., Bouhaddou, M., Xu, J., Obernier, K., White, K.M., O’Meara, M.J.,
1172 Rezelj, V.V., Guo, J.Z., Swaney, D.L., et al. (2020a). A SARS-CoV-2 protein interaction map
1173 reveals targets for drug repurposing. *Nature*.
- 1174 Gordon, D.E., Hiatt, J., Bouhaddou, M., Rezelj, V.V., Ulferts, S., Braberg, H., Jureka, A.S.,
1175 Obernier, K., Guo, J.Z., Batra, J., et al. (2020b). Comparative host-coronavirus protein
1176 interaction networks reveal pan-viral disease mechanisms. *Science*.
- 1177 Hart, T., Chandrashekar, M., Aregger, M., Steinhart, Z., Brown, K.R., MacLeod, G., Mis, M.,
1178 Zimmermann, M., Fradet-Turcotte, A., Sun, S., et al. (2015). High-Resolution CRISPR Screens
1179 Reveal Fitness Genes and Genotype-Specific Cancer Liabilities. *Cell* *163*, 1515–1526.
- 1180 Hawkins, J.L., Robbins, M.D., Warren, L.C., Xia, D., Petras, S.F., Valentine, J.J., Varghese, A.H.,
1181 Wang, I.-K., Subashi, T.A., Shelly, L.D., et al. (2008). Pharmacologic inhibition of site 1 protease
1182 activity inhibits sterol regulatory element-binding protein processing and reduces lipogenic
1183 enzyme gene expression and lipid synthesis in cultured cells and experimental animals. *J.*
1184 *Pharmacol. Exp. Ther.* *326*, 801–808.
- 1185 Hegedűs, K., Takáts, S., Boda, A., Jipa, A., Nagy, P., Varga, K., Kovács, A.L., and Juhász, G. (2016).
1186 The Ccz1-Mon1-Rab7 module and Rab5 control distinct steps of autophagy. *Mol. Biol. Cell* *27*,
1187 3132–3142.
- 1188 van der Hoek, L. (2007). Human coronaviruses: what do they cause? *Antivir. Ther.* *12*, 651–658.
- 1189 Hoffmann, H.-H., Schneider, W.M., Rozen-Gagnon, K., Miles, L.A., Schuster, F., Razoooky, B.,
1190 Jacobson, E., Wu, X., Yi, S., Rudin, C.M., et al. (2020a). TMEM41B is a pan-flavivirus host factor.
1191 *BioRxiv* 2020.10.09.334128.
- 1192 Hoffmann, M., Kleine-Weber, H., and Pöhlmann, S. (2020b). A Multibasic Cleavage Site in the
1193 Spike Protein of SARS-CoV-2 Is Essential for Infection of Human Lung Cells. *Mol. Cell* *78*, 779-
1194 784.e5.
- 1195 Hoffmann, M., Kleine-Weber, H., Schroeder, S., Krüger, N., Herrler, T., Erichsen, S., Schiergens,
1196 T.S., Herrler, G., Wu, N.-H., Nitsche, A., et al. (2020c). SARS-CoV-2 Cell Entry Depends on ACE2
1197 and TMPRSS2 and Is Blocked by a Clinically Proven Protease Inhibitor. *Cell* *181*, 271-280.e8.
- 1198 Hofmann, H., Pyrc, K., van der Hoek, L., Geier, M., Berkhout, B., and Pöhlmann, S. (2005).
1199 Human coronavirus NL63 employs the severe acute respiratory syndrome coronavirus receptor
1200 for cellular entry. *Proc. Natl. Acad. Sci. U. S. A.* *102*, 7988–7993.

- 1201 Höglinger, D., Burgoyne, T., Sanchez-Heras, E., Hartwig, P., Colaco, A., Newton, J., Futter, C.E.,
1202 Spiegel, S., Platt, F.M., and Eden, E.R. (2019). NPC1 regulates ER contacts with endocytic
1203 organelles to mediate cholesterol egress. *Nat. Commun.* *10*, 4276.
- 1204 Hsiao, T., Conant, D., Rossi, N., Maures, T., Waite, K., Yang, J., Joshi, S., Kelso, R., Holden, K.,
1205 Enzmann, B.L., et al. (2019). Inference of CRISPR Edits from Sanger Trace Data. *BioRxiv* 251082.
- 1206 Hulswit, R.J.G., Lang, Y., Bakkers, M.J.G., Li, W., Li, Z., Schouten, A., Ophorst, B., van Kuppeveld,
1207 F.J.M., Boons, G.-J., Bosch, B.-J., et al. (2019). Human coronaviruses OC43 and HKU1 bind to 9-
1208 O-acetylated sialic acids via a conserved receptor-binding site in spike protein domain A. *Proc.*
1209 *Natl. Acad. Sci. U. S. A.* *116*, 2681–2690.
- 1210 Jefferies, H.B.J., Cooke, F.T., Jat, P., Boucheron, C., Koizumi, T., Hayakawa, M., Kaizawa, H.,
1211 Ohishi, T., Workman, P., Waterfield, M.D., et al. (2008). A selective PIKfyve inhibitor blocks
1212 PtdIns(3,5)P(2) production and disrupts endomembrane transport and retroviral budding.
1213 *EMBO Rep.* *9*, 164–170.
- 1214 Jiang, P., Nishimura, T., Sakamaki, Y., Itakura, E., Hatta, T., Natsume, T., and Mizushima, N.
1215 (2014). The HOPS complex mediates autophagosome-lysosome fusion through interaction with
1216 syntaxin 17. *Mol. Biol. Cell* *25*, 1327–1337.
- 1217 Johannessen, C.M., Boehm, J.S., Kim, S.Y., Thomas, S.R., Wardwell, L., Johnson, L.A., Emery,
1218 C.M., Stransky, N., Cogdill, A.P., Barretina, J., et al. (2010). COT drives resistance to RAF
1219 inhibition through MAP kinase pathway reactivation. *Nature* *468*, 968–972.
- 1220 Kamisuki, S., Mao, Q., Abu-Elheiga, L., Gu, Z., Kugimiya, A., Kwon, Y., Shinohara, T., Kawazoe, Y.,
1221 Sato, S., Asakura, K., et al. (2009). A small molecule that blocks fat synthesis by inhibiting the
1222 activation of SREBP. *Chem. Biol.* *16*, 882–892.
- 1223 Kang, Y.-L., Chou, Y., Rothlauf, P.W., Liu, Z., Soh, T.K., Cureton, D., Case, J.B., Chen, R.E.,
1224 Diamond, M.S., Whelan, S.P.J., et al. (2020). Inhibition of PIKfyve kinase prevents infection by
1225 Zaire ebolavirus and SARS-CoV-2. *Proc. Natl. Acad. Sci.*
- 1226 Katoh, Y., Shiba, Y., Mitsuhashi, H., Yanagida, Y., Takatsu, H., and Nakayama, K. (2004). Tollip
1227 and Tom1 Form a Complex and Recruit Ubiquitin-conjugated Proteins onto Early Endosomes. *J.*
1228 *Biol. Chem.* *279*, 24435–24443.
- 1229 Klein, Z.A., Takahashi, H., Ma, M., Stagi, M., Zhou, M., Lam, T.T., and Strittmatter, S.M. (2017).
1230 Loss of TMEM106B Ameliorates Lysosomal and Frontotemporal Dementia-Related Phenotypes
1231 in Progranulin-Deficient Mice. *Neuron* *95*, 281-296.e6.
- 1232 Kleinfelter, L.M., Jangra, R.K., Jae, L.T., Herbert, A.S., Mittler, E., Stiles, K.M., Wirchnianski, A.S.,
1233 Kielian, M., Brummelkamp, T.R., Dye, J.M., et al. (2015). Haploid Genetic Screen Reveals a
1234 Profound and Direct Dependence on Cholesterol for Hantavirus Membrane Fusion. *MBio* *6*,
1235 e00801.

- 1236 Lemaire, J.-F., and McPherson, P.S. (2006). Binding of Vac14 to neuronal nitric oxide synthase:
1237 Characterisation of a new internal PDZ-recognition motif. *FEBS Lett.* *580*, 6948–6954.
- 1238 Letko, M., Marzi, A., and Munster, V. (2020). Functional assessment of cell entry and receptor
1239 usage for SARS-CoV-2 and other lineage B betacoronaviruses. *Nat. Microbiol.* 1–8.
- 1240 Li, W., Moore, M.J., Vasilieva, N., Sui, J., Wong, S.K., Berne, M.A., Somasundaran, M., Sullivan,
1241 J.L., Luzuriaga, K., Greenough, T.C., et al. (2003). Angiotensin-converting enzyme 2 is a
1242 functional receptor for the SARS coronavirus. *Nature* *426*, 450–454.
- 1243 Li, W., Xu, H., Xiao, T., Cong, L., Love, M.I., Zhang, F., Irizarry, R.A., Liu, J.S., Brown, M., and Liu,
1244 X.S. (2014). MAGeCK enables robust identification of essential genes from genome-scale
1245 CRISPR/Cas9 knockout screens. *Genome Biol.* *15*, 554.
- 1246 Liby, K.T., and Sporn, M.B. (2012). Synthetic oleanane triterpenoids: multifunctional drugs with
1247 a broad range of applications for prevention and treatment of chronic disease. *Pharmacol. Rev.*
1248 *64*, 972–1003.
- 1249 Lüningschrör, P., Werner, G., Stroobants, S., Kakuta, S., Dombert, B., Sinske, D., Wanner, R.,
1250 Lüllmann-Rauch, R., Wefers, B., Wurst, W., et al. (2020). The FTLD Risk Factor TMEM106B
1251 Regulates the Transport of Lysosomes at the Axon Initial Segment of Motoneurons. *Cell Rep.*
1252 *30*, 3506-3519.e6.
- 1253 Maeda, Y., Ide, T., Koike, M., Uchiyama, Y., and Kinoshita, T. (2008). GPHR is a novel anion
1254 channel critical for acidification and functions of the Golgi apparatus. *Nat. Cell Biol.* *10*, 1135–
1255 1145.
- 1256 Maria Fimia, G., Stoykova, A., Romagnoli, A., Giunta, L., Di Bartolomeo, S., Nardacci, R.,
1257 Corazzari, M., Fuoco, C., Ucar, A., Schwartz, P., et al. (2007). Ambra1 regulates autophagy and
1258 development of the nervous system. *Nature* *447*, 1121–1125.
- 1259 Matsuda, T., and Cepko, C.L. (2004). Electroporation and RNA interference in the rodent retina
1260 in vivo and in vitro. *Proc. Natl. Acad. Sci. U. S. A.* *101*, 16–22.
- 1261 Matsuyama, S., Nao, N., Shirato, K., Kawase, M., Saito, S., Takayama, I., Nagata, N., Sekizuka, T.,
1262 Katoh, H., Kato, F., et al. (2020). Enhanced isolation of SARS-CoV-2 by TMPRSS2-expressing cells.
1263 *Proc. Natl. Acad. Sci.* *117*, 7001–7003.
- 1264 McBride, C.E., Li, J., and Machamer, C.E. (2007). The cytoplasmic tail of the severe acute
1265 respiratory syndrome coronavirus spike protein contains a novel endoplasmic reticulum
1266 retrieval signal that binds COPI and promotes interaction with membrane protein. *J. Virol.* *81*,
1267 2418–2428.
- 1268 Mei, K., and Guo, W. (2018). The exocyst complex. *Curr. Biol.* *28*, R922–R925.

- 1269 Moretti, F., Bergman, P., Dodgson, S., Marcellin, D., Claerr, I., Goodwin, J.M., DeJesus, R., Kang,
1270 Z., Antczak, C., Begue, D., et al. (2018). TMEM41B is a novel regulator of autophagy and lipid
1271 mobilization. *EMBO Rep.* *19*.
- 1272 Olgarnier, D., Farahani, E., Thyrsted, J., Cadanet, J.B., Herengt, A., Idorn, M., Hait, A., Hernaez, B.,
1273 Knudsen, A., Iversen, M.B., et al. (2020). Identification of SARS-CoV2-mediated suppression of
1274 NRF2 signaling reveals a potent antiviral and anti-inflammatory activity of 4-octyl-itaconate and
1275 dimethyl fumarate. *BioRxiv* 2020.07.16.206458.
- 1276 Ou, X., Liu, Y., Lei, X., Li, P., Mi, D., Ren, L., Guo, L., Guo, R., Chen, T., Hu, J., et al. (2020).
1277 Characterization of spike glycoprotein of SARS-CoV-2 on virus entry and its immune cross-
1278 reactivity with SARS-CoV. *Nat. Commun.* *11*, 1620.
- 1279 Petersen, E., Koopmans, M., Go, U., Hamer, D.H., Petrosillo, N., Castelli, F., Storgaard, M.,
1280 Khalili, S.A., and Simonsen, L. (2020). Comparing SARS-CoV-2 with SARS-CoV and influenza
1281 pandemics. *Lancet Infect. Dis.* *0*.
- 1282 Petersen, J., Drake, M.J., Bruce, E.A., Riblett, A.M., Didigu, C.A., Wilen, C.B., Malani, N., Male, F.,
1283 Lee, F.-H., Bushman, F.D., et al. (2014). The Major Cellular Sterol Regulatory Pathway Is
1284 Required for Andes Virus Infection. *PLoS Pathog.* *10*.
- 1285 Puschnik, A.S., Majzoub, K., Ooi, Y.S., and Carette, J.E. (2017). A CRISPR toolbox to study virus-
1286 host interactions. *Nat. Rev. Microbiol.* *15*, 351–364.
- 1287 Ran, F.A., Hsu, P.D., Wright, J., Agarwala, V., Scott, D.A., and Zhang, F. (2013). Genome
1288 engineering using the CRISPR-Cas9 system. *Nat. Protoc.* *8*, 2281–2308.
- 1289 Rapiteanu, R., Davis, L.J., Williamson, J.C., Timms, R.T., Luzio, J.P., and Lehner, P.J. (2016). A
1290 Genetic Screen Identifies a Critical Role for the WDR81-WDR91 Complex in the Trafficking and
1291 Degradation of Tetherin. *Traffic* *17*, 940–958.
- 1292 Riva, L., Yuan, S., Yin, X., Martin-Sancho, L., Matsunaga, N., Pache, L., Burgstaller-Muehlbacher,
1293 S., De Jesus, P.D., Teriete, P., Hull, M.V., et al. (2020). Discovery of SARS-CoV-2 antiviral drugs
1294 through large-scale compound repurposing. *Nature* 1–11.
- 1295 Ronan, B., Flamand, O., Vescovi, L., Dureuil, C., Durand, L., Fassy, F., Bachelot, M.-F., Lambertson,
1296 A., Mathieu, M., Bertrand, T., et al. (2014). A highly potent and selective Vps34 inhibitor alters
1297 vesicle trafficking and autophagy. *Nat. Chem. Biol.* *10*, 1013–1019.
- 1298 Rong, Y., McPhee, C.K., Deng, S., Huang, L., Chen, L., Liu, M., Tracy, K., Baehrecke, E.H., Yu, L.,
1299 and Lenardo, M.J. (2011). Spinster is required for autophagic lysosome reformation and mTOR
1300 reactivation following starvation. *Proc. Natl. Acad. Sci.* *108*, 7826–7831.
- 1301 Rousseaux, M.W., de Haro, M., Lasagna-Reeves, C.A., De Maio, A., Park, J., Jafar-Nejad, P., Al-
1302 Ramahi, I., Sharma, A., See, L., Lu, N., et al. (2016). TRIM28 regulates the nuclear accumulation
1303 and toxicity of both alpha-synuclein and tau. *ELife* *5*.

- 1304 Saftig, P., and Klumperman, J. (2009). Lysosome biogenesis and lysosomal membrane proteins:
1305 trafficking meets function. *Nat. Rev. Mol. Cell Biol.* *10*, 623–635.
- 1306 Sanjana, N.E., Shalem, O., and Zhang, F. (2014). Improved vectors and genome-wide libraries for
1307 CRISPR screening. *Nat. Methods* *11*, 783–784.
- 1308 Schneider, W.M., Luna, J.M., Hoffmann, H.-H., Sánchez-Rivera, F.J., Leal, A.A., Ashbrook, A.W.,
1309 Pen, J.L., Michailidis, E., Ricardo-Lax, I., Peace, A., et al. (2020). Genome-scale identification of
1310 SARS-CoV-2 and pan-coronavirus host factor networks. *BioRxiv* 2020.10.07.326462.
- 1311 Shirato, K., Kawase, M., and Matsuyama, S. (2013). Middle East Respiratory Syndrome
1312 Coronavirus Infection Mediated by the Transmembrane Serine Protease TMPRSS2. *J. Virol.* *87*,
1313 12552–12561.
- 1314 Shisheva, A. (2012). PIKfyve and its Lipid Products in Health and in Sickness. In
1315 Phosphoinositides and Disease, M. FALASCA, ed. (Dordrecht: Springer Netherlands), pp. 127–
1316 162.
- 1317 Simmons, G., Gosalia, D.N., Rennekamp, A.J., Reeves, J.D., Diamond, S.L., and Bates, P. (2005).
1318 Inhibitors of cathepsin L prevent severe acute respiratory syndrome coronavirus entry. *Proc.*
1319 *Natl. Acad. Sci.* *102*, 11876–11881.
- 1320 Stewart, S.A., Dykxhoorn, D.M., Palliser, D., Mizuno, H., Yu, E.Y., An, D.S., Sabatini, D.M., Chen,
1321 I.S.Y., Hahn, W.C., Sharp, P.A., et al. (2003). Lentivirus-delivered stable gene silencing by RNAi in
1322 primary cells. *RNA N. Y. N* *9*, 493–501.
- 1323 Ströh, L.J., and Stehle, T. (2014). Glycan Engagement by Viruses: Receptor Switches and
1324 Specificity. *Annu. Rev. Virol.* *1*, 285–306.
- 1325 Stukalov, A., Girault, V., Grass, V., Bergant, V., Karayel, O., Urban, C., Haas, D.A., Huang, Y.,
1326 Oubraham, L., Wang, A., et al. (2020). Multi-level proteomics reveals host-perturbation
1327 strategies of SARS-CoV-2 and SARS-CoV. *BioRxiv* 2020.06.17.156455.
- 1328 Su, G., Kuchinsky, A., Morris, J.H., States, D.J., and Meng, F. (2010). GLay: Community structure
1329 analysis of biological networks. *Bioinformatics*.
- 1330 Sungnak, W., Huang, N., Bécavin, C., Berg, M., Queen, R., Litvinukova, M., Talavera-López, C.,
1331 Maatz, H., Reichart, D., Sampaziotis, F., et al. (2020). SARS-CoV-2 entry factors are highly
1332 expressed in nasal epithelial cells together with innate immune genes. *Nat. Med.* *26*, 681–687.
- 1333 V'kovski, P., Gerber, M., Kelly, J., Pfaender, S., Ebert, N., Braga Lagache, S., Simillion, C.,
1334 Portmann, J., Stalder, H., Gaschen, V., et al. (2019). Determination of host proteins composing
1335 the microenvironment of coronavirus replicase complexes by proximity-labeling. *ELife* *8*,
1336 e42037.

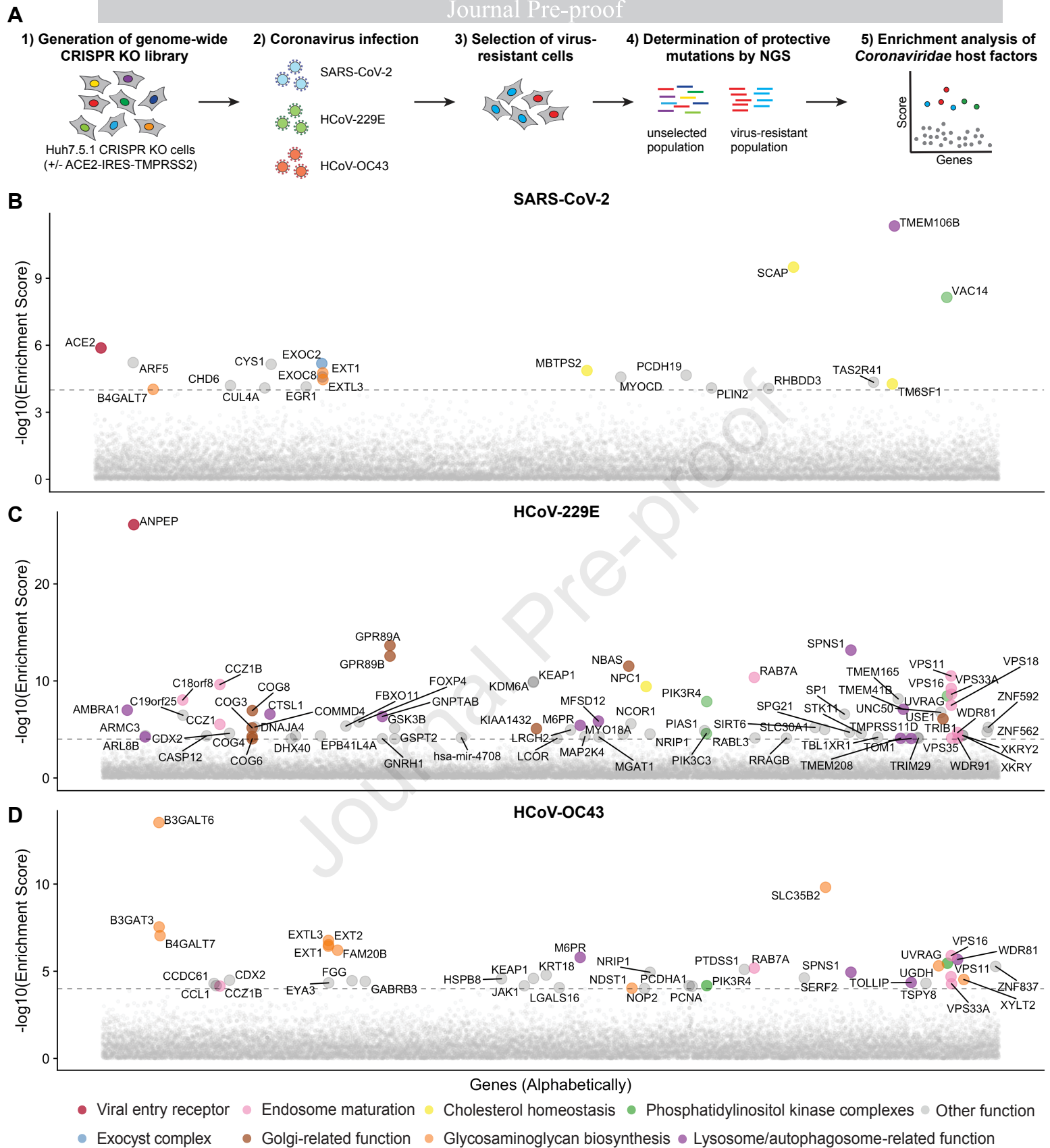
- 1337 Wei, J., Alfajaro, M.M., DeWeirdt, P.C., Hanna, R.E., Lu-Culligan, W.J., Cai, W.L., Strine, M.S.,
1338 Zhang, S.-M., Graziano, V.R., Schmitz, C.O., et al. (2020). Genome-wide CRISPR Screens Reveal
1339 Host Factors Critical for SARS-CoV-2 Infection. *Cell*.
- 1340 Wu, F., Zhao, S., Yu, B., Chen, Y.-M., Wang, W., Song, Z.-G., Hu, Y., Tao, Z.-W., Tian, J.-H., Pei, Y.-
1341 Y., et al. (2020). A new coronavirus associated with human respiratory disease in China. *Nature*
1342 *579*, 265–269.
- 1343 Yeager, C.L., Ashmun, R.A., Williams, R.K., Cardellichio, C.B., Shapiro, L.H., Look, A.T., and
1344 Holmes, K.V. (1992). Human aminopeptidase N is a receptor for human coronavirus 229E.
1345 *Nature* *357*, 420–422.
- 1346 Zaki, A.M., van Boheemen, S., Bestebroer, T.M., Osterhaus, A.D.M.E., and Fouchier, R.A.M.
1347 (2012). Isolation of a Novel Coronavirus from a Man with Pneumonia in Saudi Arabia. *N. Engl. J.*
1348 *Med.* *367*, 1814–1820.
- 1349 Zang, R., Case, J.B., Castro, M.F.G., Liu, Z., Zeng, Q., Zhao, H., Son, J., Rothlauf, P.W., Hou, G.,
1350 Bose, S., et al. (2020). Cholesterol 25-hydroxylase suppresses SARS-CoV-2 replication by
1351 blocking membrane fusion. *BioRxiv* 2020.06.08.141077.
- 1352 Zhang, X.-J., Qin, J.-J., Cheng, X., Shen, L., Zhao, Y.-C., Yuan, Y., Lei, F., Chen, M.-M., Yang, H., Bai,
1353 L., et al. (2020). In-Hospital Use of Statins Is Associated with a Reduced Risk of Mortality among
1354 Individuals with COVID-19. *Cell Metab.* *32*, 176-187.e4.
- 1355 Zhong, J., Gastaminza, P., Cheng, G., Kapadia, S., Kato, T., Burton, D.R., Wieland, S.F., Uprichard,
1356 S.L., Wakita, T., and Chisari, F.V. (2005). Robust hepatitis C virus infection in vitro. *Proc. Natl.*
1357 *Acad. Sci. U. S. A.* *102*, 9294–9299.
- 1358 Zhu, Y., Feng, F., Hu, G., Wang, Y., Yu, Y., Zhu, Y., Xu, W., Cai, X., Sun, Z., Han, W., et al. (2020).
1359 The S1/S2 boundary of SARS-CoV-2 spike protein modulates cell entry pathways and
1360 transmission. *BioRxiv* 2020.08.25.266775.
- 1361

Highlights

- Genome-wide CRISPR screens for SARS-CoV-2, HCoV-229E and HCoV-OC43 host factors
- Screens correctly identified divergent entry factors for the three coronaviruses
- Cholesterol and phosphatidylinositol pathways are shared host dependency factors
- Pharmacological inhibition of host factors reduces coronavirus replication

In brief

To identify host factors required for the infection with SARS-CoV-2 and the common cold coronaviruses OC43 and 229E, Wang et al. conduct genome-wide CRISPR knockout screens. In addition to virus-specific entry factors they uncover shared host pathways, including cholesterol homeostasis and phosphatidylinositol kinases, required for the infection with all three viruses, and demonstrate that pharmacological inhibition of these pathways exhibits pan-coronavirus antiviral activity.

Figure 1


A

9	9	2	Heparan sulfate proteoglycan biosynthetic process
13	10	2	Proteoglycan biosynthetic process
16	3	22	Vacuolar transport
13	2	19	Lysosomal transport
9	1	13	Endosome to lysosome transport
15	8	6	Aminoglycan biosynthetic process
17	10	7	Aminoglycan metabolic process
23	15	20	Glycoprotein biosynthetic process
16	3	12	Homophilic cell adhesion via plasma membrane
8	1	5	Protein targeting to vacuole
8	1	5	Selective autophagy
6	4	2	Positive regulation of interleukin 17 production
6	4	4	Chondroitin sulfate proteoglycan biosynthetic process
8	3	6	Protein localization to vacuole
18	5	15	Cell cell adhesion via plasma membrane
5	5	3	Protein targeting to lysosome
15	3	5	Response to interleukin 1
8	1	4	Positive regulation of macroautophagy
29	9	3	Process utilizing autophagic mechanism
12	9	18	Vacuole organization
6	5	10	Lytic vacuole organization
3	2	7	Intra golgi vesicle mediated transport
6	13	7	Phosphatidylinositol metabolic process
8	19	17	Golgi vesicle transport
5	10	6	Phosphatidylinositol biosynthetic process
10	17	14	Glycerophospholipid metabolic process

OC43 SARS-CoV-2 229E

Enrichment

0 2 4 6
-log₁₀(adj.p)

